Astroparticle Physics 165 (2025) 103057

Contents lists available at ScienceDirect

Astroparticle Physics

journal homepage: www.elsevier.com/locate/astropartphys

An end-to-end calibration of the Mini-EUSO detector in space

M. Battisti [a,b,*], M. Bertaina [b,c,**], E. Parizot [a,*], M. Abrate [b,c], D. Barghini [b,c,d], A. Belov [e,f], F. Bisconti [g], C. Blaksley [h], S. Blin [a], F. Capel [i], M. Casolino [g,h,j], I. Churilo [k], A.G. Coretti [b,c], M. Crisconio [l], C. De La Taille [m], T. Ebisuzaki [h], F. Fenu [l], M.A. Franceschi [n], C. Fuglesang [o], S. Gallian [b], D. Gardiol [d], A. Golzio [b,c,p], P. Gorodetzky [a], F. Kajino [q], H. Kasuga [h], P. Klimov [e], V. Kungel [r], V. Kuznetsov [k], M. Manfrin [b,c], L. Marcelli [g], W. Marszał [s], G. Mascetti [l], M. Mignone [b], H. Miyamoto [b,c], A. Murashov [f], T. Napolitano [n], H. Ohmori [h], A. Olinto [t], P. Picozza [g,j], L.W. Piotrowski [u], Z. Plebaniak [g,j], G. Prévôt [a], E. Reali [g,j], F. Reynaud [b,c], M. Ricci [n], G. Romoli [g,j], S. Sharakin [f], K. Shinozaki [s], J. Szabelski [v], Y. Takizawa [h], V. Vagelli [l], G. Valentini [l], M. Vrabel [s], L. Wiencke [r], M. Zotov [f]

[a] Université Paris Cité, CNRS, Astroparticule et Cosmologie, F-75013 Paris, France
[b] INFN Section of Turin, Via P. Giuria 1, 10125 Turin, Italy
[c] Department of Physics - University of Turin, Via P. Giuria 1, Turin 10126, Italy
[d] National Institute of Astrophysics - Astrophysical Observatory of Turin, Via Osservatorio 20, Pino Torinese, 10025, Italy
[e] Faculty of Physics - Lomonosov Moscow State University, 1(2), Leninskie gory, Moscow 119991, Russia
[f] Skobeltsyn Institute of Nuclear Physics - Lomonosov Moscow State University, 1(2), Leninskie gory, Moscow 119991, Russia
[g] INFN Section of Rome Tor Vergata, Via della Ricerca Scientifica 1, 00133 Rome, Italy
[h] RIKEN, 2-1 Hirosawa Wako, Saitama 351-0198, Japan
[i] Technical University of Munich, Arcisstraße 21, 80333 Munich, Germany
[j] Department of Physics, University of Rome Tor Vergata, Via della Ricerca Scientifica 1, 00133 Rome, Italy
[k] S.P. Korolev Rocket and Space Corporation Energia, Lenin str., 4a Korolev, 141070 Moscow area, Russia
[l] ASI, Italian Space Agency, Via del Politecnico, 00133 Rome, Italy
[m] Omega, Ecole Polytechnique, CNRS/IN2P3, Rte de Saclay, 91120 Palaiseau, France
[n] INFN National Laboratories of Frascati, Via Enrico Fermi 54, 00044 Frascati, Italy
[o] KTH Royal Institute of Technology, Brinellvägen 8, 114 28 Stockholm, Sweden
[p] Arpa Piemonte, via Pio VII, 9, Turin 10135, Italy
[q] Department of Physics, Konan University, 8-9-1 Okamoto, Higashinada, Kobe, Hyogo 658-8501, Japan
[r] Department of Physics, Colorado School of Mines, 1523 Illinois St., Golden CO 80401, United States of America
[s] National Centre for Nuclear Research, Andrzeja Sołtana 7, 05-400 Otwock, Poland
[t] Department of Astronomy and Astrophysics, The University of Chicago, 5640 S. Ellis Avenue, Chicago IL 60637, United States of America
[u] Faculty of Physics, University of Warsaw, Ludwika Pasteura 5, 02-093 Warsaw, Poland
[v] Stefan Batory Academy of Applied Sciences, Stefana Batorego 64C, 96-100 Skierniewice, Poland

ARTICLE INFO

Keywords:
Calibration
Orbital detector
Flasher
GLS system
End-to-end

ABSTRACT

Mini-EUSO is a wide Field-of-View (44°×44°) telescope currently in operation from a nadir-facing Ultra-Violet (UV) transparent window in the Russian Zvezda module on the International Space Station (ISS). Mini-EUSO has been designed as a scaled-down version of the original JEM-EUSO telescope to raise its instrumentation's technological readiness level and demonstrate its observational principle, while performing multidisciplinary studies on different fields such as atmospheric science and planetology. One of Mini-EUSO main goals is the study of the UV background for future space missions employing the same concept as the original JEM-EUSO telescope, which requires an absolute calibration of the Mini-EUSO instrument. During the past years, a few observational campaigns have been completed, employing a ground-based UV flasher to perform an end-to-end calibration of the instrument. In this paper, we present the assembled UV flasher system, the operation of the field campaign and the analysis of the obtained data. The results are interpreted by the means of a parametrization of the Mini-EUSO photon counts. The end-to-end efficiency of several pixels has been obtained,

* Corresponding author at: Université Paris Cité, CNRS, Astroparticule et Cosmologie, F-75013 Paris, France.
** Corresponding author at: INFN Section of Turin, Via P. Giuria 1, 10125 Turin, Italy
E-mail addresses: battisti@apc.in2p3.fr (M. Battisti), bertaina@to.infn.it (M. Bertaina), parizot@apc.in2p3.fr (E. Parizot).

https://doi.org/10.1016/j.astropartphys.2024.103057
Received 12 July 2024; Received in revised form 3 October 2024; Accepted 7 October 2024
Available online 11 October 2024

taking into account different parameters such as the atmospheric attenuation, the optics efficiency and the multi-anode photomultiplier detection efficiency.

1. Introduction

The cosmic ray spectrum spans over more than ten orders of magnitude in energy and reaches limits well beyond those of the most powerful accelerators created by mankind. Above 10^{18} eV, these particles are called Ultra-High Energy Cosmic Rays (UHECRs). At energies above 5×10^{19} eV, UHECR sources probably involve physical processes occurring in extreme extra-galactic environments as a limited number of known astrophysical objects can satisfy the requirements imposed by the observed spectrum, composition, and lack of strong anisotropies (e.g. [1]). At this energy, the flux becomes as low as one event per century per square kilometer [2]. Therefore, huge areas are necessary to collect enough statistics for further astronomical study.

The current main goal in the field of UHECR science is to identify their astrophysical sources and composition [3]. For this, increased statistics is one of the essential requirements. A space-based detector for UHECR research has the advantage of a very large exposure and uniform coverage of the celestial sphere, unavailable to any ground-based observatory. The space-based approach is thus complementary to the ground-based approach, which in turn provides more precise results with the limitation of scarce statistics at the highest energies. The JEM-EUSO program [4] aims to bring the study of UHECRs to space. The principle of observation is based on the detection of UV light, emitted by isotropic fluorescence of atmospheric nitrogen excited by Extensive Air Showers (EASs) in Earth's atmosphere, and forward-beamed Cherenkov radiation reflected at the Earth's surface or at dense cloud tops. The JEM-EUSO program includes a rich variety of missions: EUSO-TA [5] on ground; EUSO-Balloon [6], EUSO-SPB1 [7], and EUSO-SPB2 [8] on stratospheric balloons; TUS [9] and Mini-EUSO missions [10] in space. The future of the program is the realization of the stratospheric balloon mission PBR (POEMMA Balloon with Radio) [11,12], and the space-based missions K-EUSO [13] and POEMMA [14].

One of the main goal of Mini-EUSO is to pave the way for these ambitious space missions, by providing a reliable measurement of the UV background emission that a UHECR detector from space can expect in different conditions (type of terrain, Moon phase and elevation, cloud coverage, night glow, etc.), for the first time with a spatial and temporal resolution similar to the one expected for these future missions. For this purpose, it is necessary to correlate the measured photon count rate of a given pixel to the actual ground emissivity in a given direction, namely an absolute calibration of the detector. This paper presents a procedure to obtain the calibration, by observing the light emitted from a calibrated light source on ground, in this case an UV flasher.

The idea of using calibrated ground sources to validate the key functions of a space-based mission of UHECRs is not new, but it was already conceived at the time of the original JEM-EUSO [15] mission, resulting in the Global Light System (GLS) project, which consisted of a network of ground-based Xenon flash-lamps and steered UV lasers [16]. These functions included triggering efficiency, the accuracy of intrinsic luminosity measurements, and the reconstructed pointing direction accuracy. Mini-EUSO is the first experiment in space in the framework of the JEM-EUSO program which is making use of a prototype GLS system for an end-to-end calibration.

The paper is structured in the following way. Section 2 summarizes the key elements of the detector. Section 3 provides a parametrization of the Mini-EUSO photon count rate in different conditions. Section 4 presents the definition of the efficiency based on the quantities defined in the previous Section. Section 5 describes the prototypes of the GLS project already built, with a particular focus on the flasher system employed in the measurements. Section 6 provides the calibration of the UV flasher system. Section 7 described the attempted observational campaigns. Section 8 describes the operational procedure followed to obtain the calibration. In Section 9, the number of photons produced by the flasher is obtained. Section 10 provides an estimation of the flasher photons reaching the ISS window. Finally, in Section 11 the final efficiency of the Mini-EUSO detector is derived. Conclusions and perspectives are outlined in Section 12. In addition, more details on several topics mentioned in the text are given in the Appendix. In Appendix A the flat field procedure and its parametrization are presented. In Appendix B the weather conditions encountered during the observation campaign are discussed. Finally, in Appendix C it is compared the atmospheric transmittance derived in Section 10.1 through the application of an optical model with the observation results by the cameras of the PRISMA project [17,18], devoted to the study of bright meteors over the Italian territory.

2. The Mini-EUSO detector on board the international space station

Mini–EUSO (Multiwavelength Imaging New Instrument for the Extreme Universe Space Observatory, known as *UV atmosphere* in the Russian Space Program) [10] is a telescope operating in the near UV range, predominantly between 290 nm and 430 nm, with a square focal surface resulting in a Field of View (FoV) of $\sim 44° \times 44°$ corresponding on ground to a square of $\sim(350 \times 350)$ km^2. Its spatial resolution at ground level is approximately (5.9×5.9) km^2, slightly varying with the altitude of the ISS and the pointing direction of the pixel. The detector size is $(37 \times 37 \times 62)$ cm^3, mainly constrained by the size of the nadir-facing UV transparent window in the Russian Zvezda module, where it is attached approximately a couple of times per month during on-board night-time. The instrument has been on-board the ISS, in the Russian segment, since August 2019, thanks to a specific agreement negotiated and signed between the Italian Space Agency (ASI) and the Russian State Space Corporation, named Roscomos. The first observations took place on October 7, 2019. Since then more than 100 sessions have been performed. Data are stored locally on USB pen-drives. After each data-taking session, samples of data (about 10% of stored data, usually corresponding to the beginning and the end of each session) are copied and transmitted to ground to verify the correct functioning of the instrument and subsequently optimize its working parameters. The pouches containing all stored data are then returned to Earth on the first occasion. Currently, only the data up to session 44 are fully available on ground.

One of the main goals of Mini-EUSO is to measure the UV emissions from the ground and atmosphere and to assess the feasibility and performance of the measurement of UHECRs by means of a space-based detector [19].

Fig. 1 shows the schematic view of the Mini-EUSO telescope. The optics is based on two 25 cm diameter Fresnel lenses in PolyMethilMethAcrilate (PMMA). The Mini-EUSO focal surface, called Photo Detection Module (PDM), consists of a grid of 36 Multi-Anode Photomultiplier Tubes (MAPMTs, Hamamatsu Photonics R11265-M64) arranged in an array of (6×6) elements. Each MAPMT consists of (8×8) pixels, resulting in a total of 2304 channels. The MAPMTs are grouped in Elementary Cells (ECs) of (2×2) MAPMTs. MAPMTs are separated by 2–3 mm spacing to avoid vibration damage at launch. Consequently, gaps exist between MAPMTs in the collected images. Each EC has an independent High-Voltage Power Supply (HVPS) and board connecting

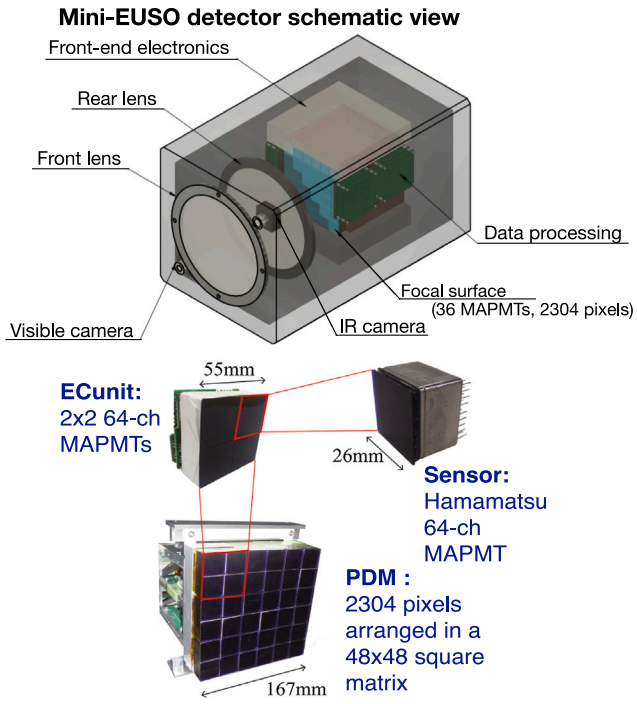

Fig. 1. Schematic view of Mini-EUSO telescope (top) and the PDM (bottom).

the dynodes and anodes of the four photomultipliers. The HVPS system is based on a Cockroft–Walton circuit. The effective focal length of the system is 300 mm, with a Point Spread Function (PSF, defined as the full width at half maximum of the distribution) of 1.2 pixels. UV bandpass filters (2 mm of BG3 material) with anti-reflective coating are glued in front of the MAPMTs to predominantly select wavelengths between 290 nm and 430 nm. The system has single photon-counting capability, meaning it can detect each photon reaching the focal plane with a given probability (photo-detection efficiency). All the plots of this work therefore show the number of "measured photon counts", from which it will be possible to deduce the number of "emitted photon counts" once the efficiency is known. The total efficiency of a pixel i (denoted as η_i) is obviously linked to its photo-detection efficiency (denoted as ξ_i) as derived in Section 4. The readout system has a double pulse resolution (defined as the minimum time distance required between two photo-electrons to be counted as two different photons) of ~6 ns. Detected photon counts are integrated over 2.5 μs Gate Time Units (GTUs) composed of 2.45 μs of active time frames followed by 50 ns dead time windows required for the ASIC readout. Mini-EUSO features a multi-level data acquisition system that stores data at three different timescales at the same time. The fastest one, called D1, (2.5 μs resolution) is used for very fast events like the search for UHECR candidates [20] and fast atmospheric Transient Luminous Events (TLEs) such as elves (Emission of Light and Very low-frequency perturbations due to E.m.p. Sources) [21]. The intermediate, called D2 (320 μs resolution), is used for the study of longer atmospheric events. Both D1 and D2 feature an autonomous trigger system [22,23]. Finally, the longer timescale, called D3 (40.96 ms time resolution) takes data continuously, resulting in slightly less than 25 frames per second. It performs a continuous monitoring of the UV emission from the Earth. It is used for the creation of UV maps [19], the observation of slow events such as meteors [24], and the monitoring of the cloud coverage. Only D3 data is used in this work. The photon counts shown in each plot or quoted in the text have been rescaled to 2.5 μs (one D1 GTU) implying that a pixel that shows 1 count in D3 has detected 16 384 photo-electrons in 40.96 ms.

3. Parametrization of Mini-EUSO photon count rate

The main goal of this work is the calibration of the Mini-EUSO instrument, which implies to obtain the correlation between the observed photon count rate and the number of photons received. The Mini-EUSO photon count rate, $\dot{N}_i(t)$, recorded at time t by pixel i observing regions characterized by an emissivity $\mathcal{E}_{\rm ph}(\theta_{\rm e}, \phi_{\rm e}, \vec{r}, t_{\rm e})$, is defined as the number of photons in the waveband of interest for Mini-EUSO emitted from the position $\vec{r}$ at time $t_{\rm e}$ per unit time ($\mathrm{d}t$), unit area ($\mathrm{d}S$) and unit solid angle ($\mathrm{d}\Omega$) in the direction $(\theta_{\rm e}, \varphi_{\rm e})$:

$$\mathcal{E}_{\rm ph}(\theta_{\rm e}, \varphi_{\rm e}; \vec{r}, t_{\rm e}) = \frac{\mathrm{d}N_{\rm ph}}{\mathrm{d}t\,\mathrm{d}S\,\mathrm{d}\Omega}. \tag{1}$$

In the following sections we will parameterize the relation between the source emissivity and the photon count rate obtained by the Mini-EUSO instrument in a few typical cases.

3.1. Photon count rate from diffuse light sources

For diffuse light sources, the photon count rate of pixel i, namely $\dot{N}_i(t)$, is obtained as the integral of the emissivity over the solid angle through which the window of the ISS is seen from position $\vec{r}$ on the ground, $\Omega_{\rm window}(\vec{r})$, itself integrated over the sector on the ground seen by pixel i, taking into account the transmission factor of the photons emitted from position $\vec{r}$ through the atmosphere, $T_{\rm atm}(\vec{r})$, the transmission factor through the optics (i.e. window of the ISS and telescope itself) to reach pixel i from the direction of $\vec{r}$, $T_{\rm optics}(\vec{r}; i)$, and the photo-detection efficiency of pixel i in the focal surface, ξ_i, defined as the ratio between the number of counts recorded by a pixel and the number of photons hitting it. We thus have:

$$\dot{N}_i(t) = \iint_{\rm ground} \mathrm{d}^2\vec{r} \int_{\Omega_{\rm window}(\vec{r})} \mathrm{d}\Omega\, \mathcal{E}_{\rm ph}(\theta_{\rm e}, \varphi_{\rm e}; \vec{r}, t_{\rm e})\, T_{\rm atm}(\vec{r})\, T_{\rm optics}(\vec{r}; i)\, \xi_i\,, \tag{2}$$

where $t_{\rm e} = t - D(\vec{r})/c$, with $D(\vec{r})$ being the distance from position $\vec{r}$ to the ISS window, and $(\theta_{\rm e}(\vec{r}), \varphi_{\rm e}(\vec{r}))$ corresponds to the direction in which the ISS is seen from position $\vec{r}$.

One can simplify this expression by noting that the FoV of a given pixel is small and the PSF of the optical system does not extend further than ~1 or 2 pixels away from the nominal focal point, which corresponds to a total effective FoV per pixel of less than ~3 degrees. As a consequence, the direction in which the ISS is seen from any position $\vec{r}$ contributing to the photon counts registered by a given pixel i is essentially constant, and can be referred to as (Θ_i, Φ_i), evaluated at the center of pixel i's footprint on the ground, at position $\vec{r}_i$. In particular, for pixel i, $\Omega_{\rm window}(\vec{r})$ can be replaced in Eq. (2) by the constant $\Omega_i \equiv \Omega_{\rm window}(\vec{r}_i)$, and $T_{\rm atm}(\vec{r})$ by $T_i^{\rm (atm)} \equiv T_{\rm atm}(\vec{r}_i)$. One thus obtains:

$$\dot{N}_i(t) = \left[\iint_{\rm ground} \mathrm{d}^2\vec{r}\ \mathcal{E}_{\rm ph}(\Theta_i, \Phi_i; \vec{r}, t_{\rm em})\, T_{\rm optics}(\vec{r}; i)\right] \xi_i\, \Omega_i\, T_i^{\rm (atm)}\,. \tag{3}$$

If D_i is the distance between the ISS and the position $\vec{r}_i$ on the ground, $S_{\rm window}$ the area of the entrance window on the ISS, and Θ_i the angle at which pixel i is pointing with respect to the window axis, we have:

$$\Omega_i = \frac{S_{\rm window}\cos\Theta_i}{D_i^2} = \frac{S_{\rm window}\cos^3\Theta_i}{H_{\rm ISS}^2}, \tag{4}$$

where $H_{\rm ISS} = D_i\cos\Theta_i$ is the difference in altitude between the source and the ISS at the moment of the measurement.

3.2. Uniform diffuse background

In the case of a diffuse background associated with an emissivity that is uniform, constant and isotropic, i.e. $\mathcal{E}_{\rm ph}(\theta, \phi; \vec{r}, t_{\rm em}) = \mathcal{E}_0$, the resulting number of photons counted by pixel i during one GTU, of duration $\Delta t_{\rm GTU}$, is:

$$N_i = \int_{\mathrm{GTU}} \dot{N}_i \, \mathrm{d}t = \mathcal{E}_0 \, \Delta t_{\mathrm{GTU}} \, \Omega_i \, T_i^{(\mathrm{atm})} \xi_i \times \iint_{\mathrm{ground}} \mathrm{d}^2\vec{r} \; T_{\mathrm{optics}}(\vec{r}; i). \tag{5}$$

In this formula, the integral over the area observed by pixel i is delicate to handle, because the actual PSF of the optical system is not known precisely. If the stigmatism of the optical system were perfect, i.e. if the PSF were perfectly peaked, with each position on the ground sending photons to one single pixel on the focal surface, the integral could be restricted to the area actually seen by the pixel under consideration, and one could rewrite:

$$\iint_{\mathrm{ground}} \mathrm{d}^2\vec{r} \; T_{\mathrm{optics}}(\vec{r}; i) \equiv S_i \times T_i^{(\mathrm{optics})}, \tag{6}$$

where S_i is the area of the nominal projection of the FoV of pixel i on the ground, and $T_i^{(\mathrm{optics})}$ is the throughput of the optical system (including the transparency if the ISS window, the transmittance of the two Fresnel lenses, the possible internal reflections and the obscuration of the PDM and the other ancillary devices) for incoming photons from the directions covered by pixel i.

In the case of our non-perfect PSF, a point source on the ground sends photons to the nominally conjugated pixel as well as nearby ones. Conversely, a given pixel receives photons from its nominally conjugated region on the ground, as well as from an extended region around it Therefore, the integral in Eq. (6) extends to all positions on the ground contributing to pixel i, and we can rewrite the optics transmittance from the direction of position $\vec{r}$ to pixel i as:

$$T_{\mathrm{optics}}(\vec{r}, i) = T_{\vec{r}}^{(\mathrm{optics})} \times \mathrm{PSF}(\vec{r} \to i), \tag{7}$$

where

- $T_{\vec{r}}^{(\mathrm{optics})}$ is the throughput of the whole Mini-EUSO optical system for light coming from the direction of position $\vec{r}$,
- $\mathrm{PSF}(\vec{r} \to i)$ is the fraction of all detected photons coming from that direction that are actually reaching pixel i;

Further approximating $T_{\vec{r}}^{(\mathrm{optics})}$ as $T_{\vec{r}_j}^{(\mathrm{optics})} \equiv T_j^{(\mathrm{optics})}$ for all positions $\vec{r}$ within the footprint of pixel j, we have:

$$\begin{aligned} \iint_{\mathrm{ground}} \mathrm{d}^2\vec{r} \; T_{\mathrm{optics}}(\vec{r}; i) &= \iint_{\mathrm{ground}} \mathrm{d}^2\vec{r} \; \mathrm{PSF}(\vec{r} \to i) \; T_{\vec{r}}^{(\mathrm{optics})} \\ &= \sum_j \iint_{S_j} \mathrm{d}^2\vec{r} \; \mathrm{PSF}(\vec{r} \to i) \; T_j^{(\mathrm{optics})} \\ &\equiv \sum_j S_j \, \mathrm{PSF}(j \to i) \; T_j^{(\mathrm{optics})}. \end{aligned} \tag{8}$$

where S_j is again the nominal area of the footprint of pixel j and $\mathrm{PSF}(j \to i) \equiv \langle \mathrm{PSF}(\vec{r} \to i) \rangle$ is the average spill-over of photons that would nominally reach pixel j but are actually reaching pixel i. Note that this rewriting is valid if the final sum over the pixels if performed over an area larger than the extension of the PSF on the focal surface, and thus only for pixels sufficiently far from the borders (typically ~ 2 pixels away).

We can further simplify this equation by noticing that nearby pixels cover essentially similar surfaces on the ground. Therefore, as long as the PSF is limited to a few pixels, we can write:

$$S_j = S_i \quad (\text{for } j \text{ close to } i). \tag{9}$$

The average error introduced by this approximation is essentially negligible, namely below 0.5% (0.37%) for more than 66% (50%) of the pixels if one restricts to a (5 × 5) pixel box. This can be seen in Fig. 2, where we plot the relative difference between the area of a given pixel's footprint on the ground and the average of those of the 24 closest pixels.

Likewise, we can acknowledge that nearby pixels have similar values of the optical transmission, i.e.:

$$T_j^{(\mathrm{optics})} = T_i^{(\mathrm{optics})} \quad (\text{for } j \text{ close to } i). \tag{10}$$

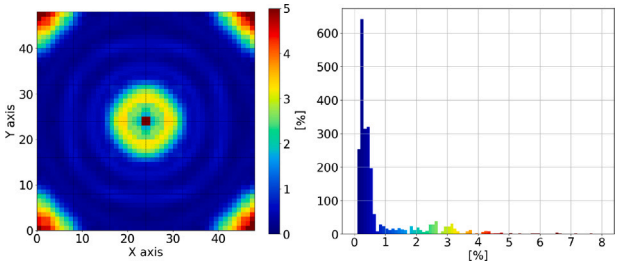

Fig. 2. Left: map of the relative difference between the surface of the footprint of a given pixel and the average surface of the footprints of its 24 closest neighbors. **Right:** histogram of the values. The color scale (in percent) is common to the two panels.

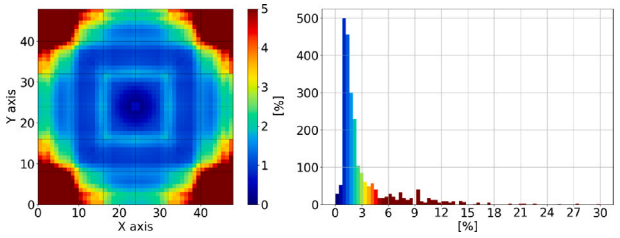

Fig. 3. Left: map of the relative difference between the PCE of a given pixel and the average PCEs of the 24 closest neighbors. **Right:** histogram of the values. The color scale (in percent) is common to the two panels. The PCE for pixel observing at an angle $\theta > 22°$ is extrapolated from the measurement presented in [5].

Fig. 3 shows that this assumption is correct within a few percent. In particular, the difference of the Photon Collection Efficiency (PCE, defined as the light collected in a square of (5×5) mm^2) is below 1.7% (3%) for 50% (75%) of the pixels if one restricts to a (5×5) pixel box.

Finally, assuming that the PSF is locally symmetric in the sense that

$$\mathrm{PSF}(j \to i) = \mathrm{PSF}(i \to j), \tag{11}$$

and further noting that, obviously:

$$\sum_j \mathrm{PSF}(i \to j) = 1, \tag{12}$$

we also have:

$$\sum_j \mathrm{PSF}(j \to i) = 1. \tag{13}$$

With the above approximations, we can then finally rewrite Eq. (5) giving the photon counts in pixel i per GTU, in the case of a uniform diffuse background with uniform emissivity $\mathcal{E}_0$, as:

$$\begin{aligned} N_i = \; & \mathcal{E}_0 \, \Delta t_{\mathrm{GTU}} \, \Omega_i \, T_i^{(\mathrm{atm})} \, \xi_i \sum_j S_j \, \mathrm{PSF}(j \to i) \, T_j^{(\mathrm{optics})} \\ \simeq \; & \mathcal{E}_0 \, \Delta t_{\mathrm{GTU}} \, \Omega_i \, T_i^{(\mathrm{atm})} \, \xi_i \, S_i \, T_i^{(\mathrm{optics})} \sum_j \mathrm{PSF}(j \to i) \\ \simeq \; & \mathcal{E}_0 \, \Delta t_{\mathrm{GTU}} \, \Omega_i \, T_i^{(\mathrm{atm})} \, S_i \, T_i^{(\mathrm{optics})} \, \xi_i. \end{aligned} \tag{14}$$

It is worth noting that the same parametrization applies to diffuse light sources not on the ground but at a higher altitude, such as clouds and airglow, simply by using the correct values for $\mathcal{E}_0$, Ω_i, $T_i^{(\mathrm{atm})}$ and S_i.

3.3. Point-like source (flasher) on the ground

The case of a point-like source at position $\vec{r}_0$ on the ground can be treated in a similar way, replacing the emissivity $\mathcal{E}_{\mathrm{ph}}(\theta_e, \varphi_e; \vec{r}, t_e)$ by the appropriate function which will include the $\delta(\vec{r} - \vec{r}_0)$ delta function to localize the source in position $\vec{r}_0$ on the ground. In the particular case of a flasher source on ground, we have:

$$\mathcal{E}_{\mathrm{ph}}(\theta_e, \varphi_e; \vec{r}, t_e) = \mathcal{Q}_{\mathrm{flasher}} \times \delta(\vec{r} - \vec{r}_0) \times f(\theta_e) \times g(t_e), \tag{15}$$

where $\mathcal{Q}_{\text{flasher}}$ is the number of photons emitted by the source (flasher) per unit time and unit solid angle in the forward direction (namely, $\theta = 0$, $\phi = 0$), $f(\theta_e)$ describes the angular modulation of the flasher (cf. Section 6.4), and $g(t_e)$ encodes the flashing sequence (cf. Section 5.2), and is equal to either 1 or 0 in our case.

Again, the signal being not entirely contained in a single pixel because of the imperfect PSF, several pixels are likely to receive light from a source located at position $\vec{r}_0$, even if this is outside their nominal FoV. With the above notations, the photon counts in pixel j from the point-like in the FoV of pixel i are given by (using Eq. (7)):

$$N_j^{(\text{flasher})} = \mathcal{Q}_{\text{flasher}}\, f(\Theta_i)\, \Delta t_{\text{GTU}}\, \Omega_i\, T_i^{(\text{atm})}\, T_i^{(\text{optics})}\, \text{PSF}(\vec{r}_0 \to j)\, \xi_j\,. \tag{16}$$

Note that the factors $f(\Theta_i)$, Ω_i, $T_i^{(\text{atm})}$ and $T_i^{(\text{optics})}$ depend on i, not on j. The above equation is valid for every pixel. Obviously, the contribution from a pixel j far away from pixel i becomes negligible due to the factor $\text{PSF}(\vec{r}_0 \to j)$ that quickly tends to 0 while moving away from pixel i.

4. Definition of the overall efficiency of a pixel

For future use in UHECR experiments from space, in particular to determine the exposure as a function of energy, we are interested in determining the background emissivity of the Earth in different conditions. Mini-EUSO can measure it, provided a proper calibration is done. The goal is to go from the measured photon counts in a given pixel to the actual ground emissivity in that direction, i.e., with the above notations, to go from N_i to $\mathcal{E}_0$. This conversion is derived from Eq. (14):

$$\mathcal{E}_0 = \frac{N_i}{\Delta t_{\text{GTU}}\, \Omega_i\, S_i\, T_i^{(\text{atm})}\, T_i^{(\text{optics})}\, \xi_i}, \tag{17}$$

where the first three quantities in the denominator are known or computable from the geometry of the ISS, the fourth one can be estimated from an atmospheric model, and the product of the last two quantities defines the light detection efficiency in the direction observed by pixel i:

$$\eta_i = T_i^{(\text{optics})} \times \xi_i\,. \tag{18}$$

4.1. Experimental procedure

In order to measure the quantity of Eq. (18), we use a calibrated light source (the *INFN Turin UV flasher*, presented in Section 5.2). We can express the photon counts produced by the flasher, $N_j^{(\text{flasher})}$, through Eq. (16). In particular, if the flasher is in the FoV of pixel i at $\vec{r}_0$:

$$N_i^{(\text{flasher})} = \mathcal{Q}_{\text{flasher}}\, f(\Theta_i)\, \Delta t_{\text{GTU}}\, \Omega_i\, T_i^{(\text{atm})}\, \eta_i\, \text{PSF}(\vec{r}_0 \to i)\,. \tag{19}$$

Unfortunately, this equation cannot be used to determine η_i from the $N_i^{(\text{flasher})}$, because the $\text{PSF}(\vec{r}_0 \to i)$ is not known precisely, and strongly depends on the position $\vec{r}_0$ within the pixel. However, we can integrate the flasher signal over a larger area on the focal surface, to cover most of the PSF, and thus reduce the dependence on its actual shape and on $\vec{r}_0$. However, in order to sum the photon counts coming from the flasher in different pixels, we need to take into account their different intrinsic photo-detection efficiencies. Although these are not known (since this is what we want to determine), their *ratio* can be obtained from the analysis of their response to uniform light, which is all we need here.

Indeed, from Eq. (14), the ratio of the photon counts from pixel i and pixel j observing a common uniform background, $\mathcal{E}_0$, is given by:

$$\frac{N_i^{\text{bkg}}}{N_j^{\text{bkg}}} = \frac{\Omega_i\, T_i^{(\text{atm})}\, S_i\, T_i^{(\text{optics})}\, \xi_i}{\Omega_j\, T_j^{(\text{atm})}\, S_j\, T_j^{(\text{optics})}\, \xi_j} \simeq \frac{\xi_i}{\xi_j}, \tag{20}$$

where the last equality holds for nearby pixels, as discussed above.

The knowledge of this ratio allows us to compute a new quantity, defined as the sum of the photon counts of all pixels in a (5×5) pixel box centered around the pixel i, rescaled by their respective intrinsic efficiencies, which we denote by $N_i^{(5\times5)}$:

$$\begin{aligned} N_i^{(5\times5)} &= \sum_{j \in \text{Box}(i)} \frac{\xi_i}{\xi_j} \times N_j^{(\text{flasher})} \\ &= \mathcal{Q}_{\text{flasher}}\, f(\Theta_i)\, \Delta t_{\text{GTU}}\, \Omega_i\, T_i^{(\text{atm})} \times T_i^{(\text{optics})}\, \xi_i \sum_{j \in \text{Box}(i)} \text{PSF}(\vec{r}_0 \to j). \end{aligned} \tag{21}$$

From this, we can finally obtain:

$$\begin{aligned} \eta_i &= T_i^{(\text{optics})}\, \xi_i \\ &= \frac{N_i^{(5\times5)}}{\mathcal{Q}_{\text{flasher}}\, f(\Theta_i)\, \Delta t_{\text{GTU}}\, \Omega_i\, T_i^{(\text{atm})} \sum_{j\in\text{Box}(i)} \text{PSF}(\vec{r}_0 \to j)} \\ &\simeq \frac{N_i^{(5\times5)}}{\mathcal{Q}_{\text{flasher}}\, f(\Theta_i)\, \Delta t_{\text{GTU}}\, \Omega_i\, T_i^{(\text{atm})}} \end{aligned} \tag{22}$$

where the last equality assumes that ~100% of the signal from the flasher is contained within the (5×5) box.

The denominator can be recognized as the number of photons reaching the window of the ISS from the flasher. Noting $N_i^{(\text{window})}$ this number, we thus have a new, operational expression for the pixel efficiency:

$$\eta_i = \frac{N_i^{(5\times5)}}{N_i^{(\text{window})}}. \tag{23}$$

4.2. Efficiency ratios

As it can be seen explicitly on Eq. (21), the completion of the calibration procedure with the flasher requires a knowledge of the relative pixel response to a common uniform background. This is required locally to obtain the absolute calibration of the pixels seeing the flashes, and it can also be used globally to extend this absolute calibration of a few pixels to the entire focal surface. Thus, a key element of the analysis (apart from the characterization of the flasher itself and from the measurement of photon counts) is the evaluation of the efficiency ratios (between individual pixels). This is usually done through the observation of a so-called "flat field", with all pixels observing the same light. In the case of Mini-EUSO, this could not be done on the ground before launch, and in any case it would still have needed to be updated in flight, taking into account the (angular-dependent) transparency of the ISS window, as well as the possible pixel-dependent ageing of the photo-detectors. Observing a flat field in flight is also not possible, given the very large FoV of the instrument. Therefore, we use an "asynchronous" flat fielding procedure to determine the individual response of the different pixels to an (approximately) identical ground emissivity, even though this reference ground emissivity, $\mathcal{E}_{\text{ref}}$, is not observed at the same time by all pixels.

This flat fielding procedure is described in [19] and summarized in Appendix A, using the physical quantities $T_i^{(\text{optics})}$, $T_i^{(\text{atm})}$, Ω_i, S_i and ξ_i introduced in the present paper.

5. The Global Light System (GLS)

A scaled version of the JEM-EUSO GLS system has been developed to test the expected energy threshold and performance of Mini-EUSO. It consists of a mobile, steerable UV laser system and several ground-based flashers.

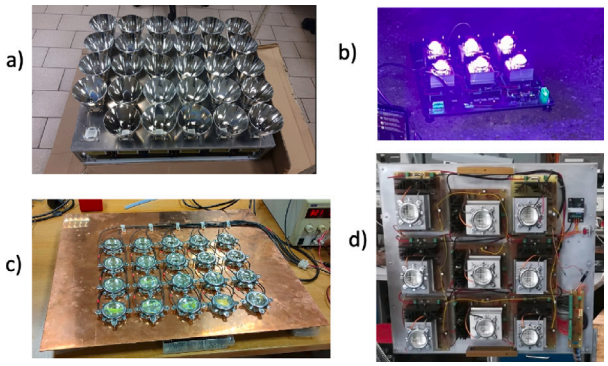

Fig. 4. Pictures of the available flasher systems. (a) *RIKEN UV flasher*, developed in Japan, (b) *APC UV flasher*, developed in France, (c) *INFN Rome flasher*, developed in Italy (d) *INFN Turin UV flasher*, developed in Italy.

5.1. The UV laser

The steerable UV laser system has been developed at Colorado School of Mines. Housed in a customized trailer, a calibrated pulsed 355 nm frequency-tripled Yttrium Aluminum Garnet (YAG) laser, has an energy range from 200 μJ to 90 mJ [25]. It can emit pulsed 355 nm UV laser light to produce a short speed-of-light track in the detector. The brightness of this track is similar to the track from an EAS resulting from a cosmic ray of up to 10^{21} eV. The energy calibration factor is stable within 5%. The laser beam can reach any direction above the horizon with a pointing accuracy higher than $\pm 0.1°$. The laser system will be driven to remote locations in the Western US and aimed across the FoV of Mini-EUSO when the ISS passes overhead during dark nights. Unfortunately, up to now it was not possible to operate the system but it is planned to make use of it as soon as the logistics, a suitable orbit, and weather conditions will allow.

5.2. The UV flashers

At the same time, several ground-based flashers have been developed in different groups of the JEM-EUSO collaboration (in Japan, Italy, and France). Fig. 4 shows examples of these systems. The *INFN Rome flasher*, based on an array of 20 white LEDs, was tested on several occasions but it turned out to be at the detection limit. The *RIKEN UV flasher* could not be operated due to adverse meteorological and orbit conditions. The *APC UV flasher*, developed at the Astroparticule at Cosmologie (APC) laboratory, in Paris, is made of two arrays of 9 UV LEDs that can either fire independently or together. It was developed only recently and successfully tested. The two arrays of the *APC UV flasher* are an exact replica of the *INFN Turin UV flasher*, presented in the next Section.

5.3. INFN Turin UV flasher

The *INFN Turin UV flasher* is the known ground source used to perform the end-to-end calibration of the Mini-EUSO telescope. Its calibration procedure is presented in Section 6.

The *INFN Turin UV flasher* consists of an array of 9 100 W COB-UV LEDs driven by an Arduino board, powered through 3 lead-ion batteries connected in series, providing a nominal tension of 38 V. Each UV LED comes with its own lens and emits photons in a very narrow bandwidth, peaked around (400 ± 5) nm,[1] as shown in Fig. 5. This measurement has been performed through a high-precision spectrometer hosted at the APC laboratory. All LEDs are fixed on a plate parallel to each other, with the axis of their lens perpendicular to the plate. This common axis is used as a reference for pointing, i.e. directions in space are indicated by a polar angle, θ, and an azimuth φ, the flasher's axis itself corresponding to $\theta = 0$ and $\varphi = 0$. Given the symmetries of the system, no dependence in φ is expected.

[1] The uncertainty of 5 nm represents the half-width at half maximum of the distribution.

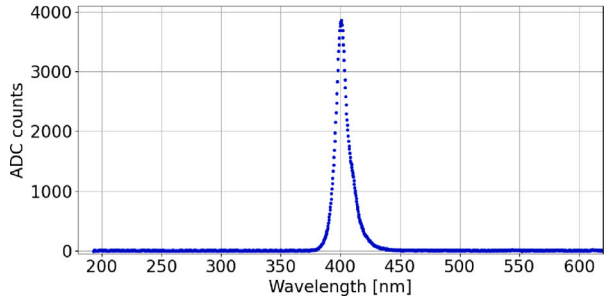

Fig. 5. Spectrum of the UV LEDs used to assemble the *INFN Turin UV flasher* and the *APC UV flasher*.

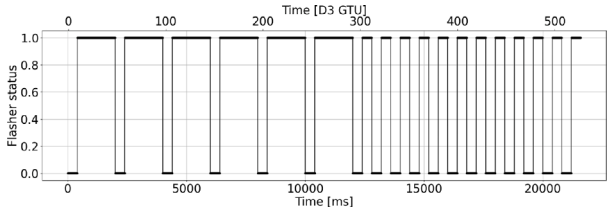

Fig. 6. Pattern of the *INFN Turin UV flasher*. The entire cycle lasts for 21.6 s, slightly less than half of the time a ground source takes to cross the entire Mini-EUSO FoV.

The pattern of the *INFN Turin UV flasher* was chosen to maximize the probability of observing the flasher from the center of a pixel FoV. Assuming an average velocity of $v_{ISS} = 7.7$ km/s, the ISS takes roughly 820 ms to travel the distance corresponding to the footprint of a pixel. In other words, the FoV of a Mini-EUSO pixel changes completely every 820 ms, roughly 20 D3 GTUs. It has been, therefore, decided to alternate long and short pulses: the long pulses (of almost 40 D3 GTUs) guarantee that the flasher "crosses" the entire FoV of at least one pixel, while the short pulses (10 D3 GTUs) reduce the error on the background estimation as both signal and background information can be retrieved during the period in which the flasher is in the FoV of the pixel. Moreover, such a peculiar pattern can be easily recognized in the data. Summarizing, the flasher pattern has been chosen to be 6 × [1.6 s ON + 0.4 s OFF] + 12 × [0.4 s ON + 0.4 s OFF] or, in terms of D3 GTU, 6 × [39 GTU ON + 10 GTU OFF] + 12 × [10 GTU ON + 10 GTU OFF], as shown in Fig. 6. The entire cycle lasts for 21.6 s, slightly less than half of the time a ground source takes to cross the entire Mini-EUSO FoV.

6. Calibration of the *INFN Turin UV flasher*

The *INFN Turin UV flasher* has been calibrated in laboratory measuring its emissivity Q_{Flasher}, namely the number of photons emitted by the *INFN Turin UV flasher* per unit of time and solid angle. Since instrumentation to directly measure the photons emitted was not available at the time, an indirect measurement, described in [26], was performed. A second, direct measurement was performed afterward, taking advantage of two absolutely calibrated Low-Gain Photo-diodes (LGPDs). This second measurement is presented in Section 6.2. A third, more recent, calibration performed in open-air condition is presented in Section 6.3.

Fig. 7. Left: The PD300-UV silicon photo-diode sensor used to perform the analysis. **Right:** The 7Z01701 Centauri Dual Channel Powermeter that reads out the photo-diodes.

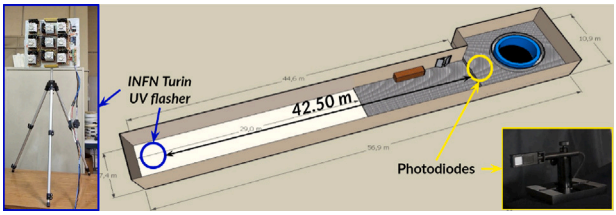

Fig. 8. Schematic view of TurLab facility where the positions of the *INFN Turin UV flasher* and the photo-diodes are indicated.

6.1. Calibration setup

6.1.1. The Low Gain Photo-diode (LGPD)

The instrumentation is made of a set of 2 LGPDs [27], read out by a dual-channel power-meter (Fig. 7). The whole system has been absolutely calibrated by the manufacturer which guarantees a linear response over a large power range (from pW to mW) and bandwidth (from 200 nm to 1100 nm). The aperture size $S_{\rm LGPD}$ is (1×1) cm^2 and the final uncertainty on the power measured is ±3%. In our case, we are interested in the number of photons received by the photo-diodes per unit of time, which can be easily obtained from the power $\mathcal{P}_{light}$ measured by the power-meter. In a monochromatic source of wavelength λ, each photon carries an energy

$$E_{ph} = \frac{hc}{\lambda} \simeq 4.966 \times 10^{-19} \left(\frac{400\ \text{nm}}{\lambda}\right)\ \text{J} \tag{24}$$

The power $\mathcal{P}_{light}$ can be converted into the rate of photons received $\dot{N}_{ph}$ through the expression

$$\dot{N}_{ph} = \frac{\mathcal{P}_{light}}{E_{ph}} \simeq \left(\frac{\mathcal{P}_{light}}{\text{W}}\right)\ 2.0137 \times 10^{18} \left(\frac{400\ \text{nm}}{\lambda}\right)\ \text{ph/s} \tag{25}$$

6.1.2. The TurLab facility

The calibration of the *INFN Turin UV flasher* is performed in the large dark room of the TurLab facility [28], located in the fourth basement of the Physics department building of the University of Turin (see Fig. 8). Here the flasher is installed on a tripod 42.50 m away and pointed towards the photo-diodes. A 60.5 cm long cardboard tube with a square section of (2.5×2.5) cm^2 is placed around one photo-diode to prevent diffuse and reflected light from reaching it. The second LGPD is placed next to the cardboard tube. The difference between the two is a measurement of the light reflected from various objects and surfaces.

6.2. Flasher emissivity in the forward direction measured in laboratory

The flasher emissivity in the forward direction $\mathcal{Q}_{\rm flasher}$, namely the number of photons emitted by the source per unit time and unit solid angle in the direction $\theta = 0$, $\phi = 0$, is needed to compute the efficiency of a pixel, as expressed in Eq. (22).

It can be computed as

$$\mathcal{Q}_{\rm flasher} = \frac{\dot{N}_{ph}}{\Omega_{\rm LGPD}} \tag{26}$$

where the photon rate $\dot{N}_{ph}$ is derived from $\mathcal{P}_{light}$ through Eq. (25) and $\Omega_{\rm LGPD}$ is the solid angle subtended by the photo-diode at the position of the flasher. The solid angle is obtained as

$$\Omega_{\rm LGPD} = \frac{S_{\rm LGPD}}{D^2_{\rm LGPD}} = \frac{1\ \text{cm}^2}{(42.50\ \text{m})^2} \simeq 5.54\ 10^{-8}\ \text{sr}, \tag{27}$$

where $S_{\rm LGPD}$ is the areas of the photo-diode and $D_{\rm LGPD}$ is the distance between the *INFN Turin UV flasher* and the LGPDs.

Fig. 9 shows the emissivity measured at TurLab for the *INFN Turin UV flasher* computed through Eq. (26), during a ∼5 min long acquisition. The top panel shows the results obtained with and without the collimator. As expected, the two measurements show the same pattern, with a difference in the intensity of ∼3% due to the light reflected and diffused from the environment that reaches the photo-diode outside the collimator. Since we are only interested in the direct emission, we will use the result obtained with the collimator (in red) to obtain the numerical value of $\mathcal{Q}_{\rm flasher}$ used in this work. The second panel shows the time evolution of the intensity of the flashes during the whole acquisition. The measured intensity is not perfectly constant, but it varies by a few percent during the acquisition. This is due to the combination of two different effects. The first one is related to the power system, the three lead-ion batteries connected in series. With the use, the charge stored in the batteries starts to deplete. When it is below a certain threshold, the current flowing through the LEDs starts decreasing, slightly reducing the light intensity of the flasher. This effect is called *charge effect*. The second effect is due to the temperature variation of the LED junction. When the flasher is switched on, the temperature starts increasing, reducing the light yield of the flasher (and slightly changing the wavelength, moving towards longer wavelengths). This effect is called *thermal effect*. In this second panel we can appreciate that the intensity decreases linearly with time, slightly reducing the light intensity by ∼1.5% over the entire measurement of almost 6 min (*charge effect*). From the plot we can obtain the average value of the emissivity of the *Turin INFN UV flasher*, which results to be 3.1×10^{20} ph/s/sr. The third panel presents a zoom over a 1-min period. It is possible to appreciate the alternation of short pulses (12 flashes in almost 10 s) and long pulses (6 flashes in 12 s), and the fact that during a pulse the intensity decreases by a factor 2%–3%. This is caused by the *thermal effect*. The average of each pulse is indicated by a blue dot. Finally, the fourth panel shows the values of the averages. The average emissivity of the short pulses is higher than the one of the long pulses, by a factor ∼2.5%. This effect is a combination of the two different causes, the charge effect and the thermal effect.

All these aforementioned effects that tend to change the intensity of the flasher light, concur to increase the uncertainty on the estimation of the flasher emissivity. An additional uncertainty factor comes from the presence of the collimator in front of the LGPD and its (mis)alignment with the flasher axis, partially compensated by the reflectivity of its internal walls. Taking everything into account we can estimate the uncertainty of the emissivity to be 8%. As mentioned above, an additional 3% comes from the intrinsic power resolution of the LGPDs. The two uncertainties are independent and treated accordingly.

We thus obtain the numerical value of the flasher emissivity in the forward direction, $(\theta, \phi) = (0, 0)$:

$$\mathcal{Q}_{\rm flasher} = (3.1 \pm 0.3) \times 10^{20}\ \text{ph/s/sr}. \tag{28}$$

6.3. Flasher emissivity in the forward direction measured in open-air conditions

As explained in Section 6.1.2, the use of a collimator was required to prevent light reflected by the walls, floor, and ceiling of the laboratory from reaching the photo-diode. This can also introduce other sources of uncertainty due to the mis-alignment of the collimator with the LGPD optical axis or the internal reflectivity of the collimator walls. To

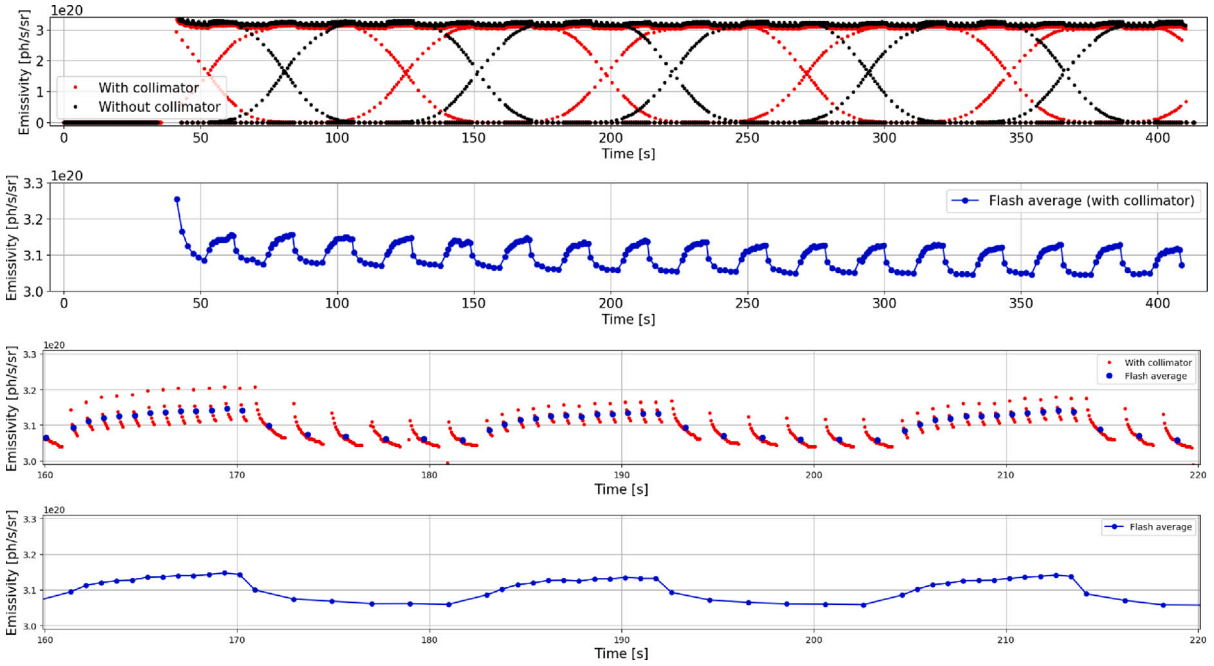

Fig. 9. Emissivity of the *Turin INFN UV flasher* measured at TurLab facility with the two low-gain photo-diodes (LGPDs), obtained through Eq. (26). **Top:** Emissivity measured by the two LGPDs placed inside (red) and outside (black) the collimator. The periodic pattern is due to aliasing effects. **Middle Top:** The average value of each flash observed by the LGPD inside the collimator. A linear decrease is present, due to the depletion of the charge of the batteries. **Middle Bottom:** Zoom over a 1 min of the collimated signal. The blue dots indicate the average value of each flash. During each flash, the intensity of the signal decreases. This is an effect of the heating of the LEDs. **Bottom:** Evolution of the average value of the flashes over the same minute. The average emissivity of the short pulses is larger than the emissivity of long pulses. This effect is a combination of the heating of the UV LEDs (thermal effect) and the batteries being unable to provide enough power for the whole duration of a pulse (charge effect).

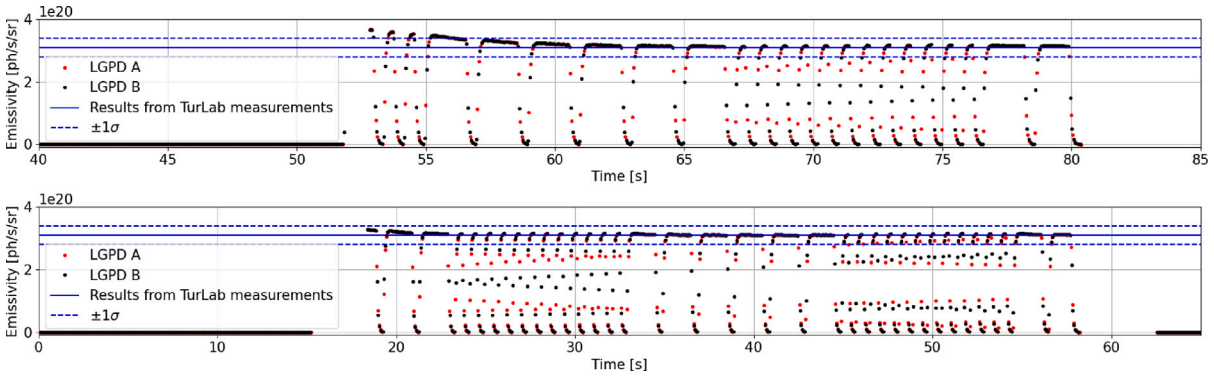

Fig. 10. Emissivity of the *Turin INFN UV flasher* measured in open-air condition. The two colors represent the output of the two LGPDs, that show the same results. The blue horizontal lines represent the value of the flasher emissivity obtained at the TurLab facility and expressed in Eq. (28). **Top:** The very first measurement, with the battery fully charged. The emissivity starts slightly higher than the reference value, but then it quickly decreases, almost reaching the reference in ~ 30 s of operation. **Bottom:** A second measurement taken after $\sim$1 min of operation. The emissivity is perfectly compatible with the result obtained at the TurLab facility.

completely remove the need for a collimator, we performed another calibration in open-air condition, in an area with direct line of sight between the LGPDs and the flasher, and without anything nearby that could scatter or reflect light. The flasher has been installed $\sim$100 m away from the photo-diodes, measuring the output for several minutes. The results are shown in Fig. 10, along with the results of $\mathcal{Q}_{\rm flasher} = (3.1 \pm 0.3) \times 10^{20}$ ph/s/sr obtained in the previous Section. As it was measured at the TurLab facility, when the batteries are fully charged, the flasher emissivity is slightly higher (Fig. 10, top), but after a few tens of seconds of operation it stabilizes to the value obtained in the laboratory (Fig. 10, bottom). As it will be briefly mentioned in Section 7, the flasher is typically switched on a couple of minutes before the foreseen ISS passage, so the "stabilized" value of Eq. (28) is the one that will be used in the rest of the paper. Measurement results acquired during "open-air" calibration run are in full agreement with the value of the emissivity obtain at the TurLab facility and presented in the previous Section.

6.4. Flasher emissivity as a function of the viewing angle

"Open-air" calibration measurements were conducted for the case when the flasher is aligned with the detector, namely the angle θ between detector's optical axis and the flasher's pointing direction is zero. We can generalize the result by introducing a factor $f(\theta)$ already mentioned in Eq. (15), that expresses the angular transmittance of the lenses mounted in front of the UV LEDs that make up the *INFN Turin UV flasher*. With this, we can express the flasher emissivity as

$$\mathcal{Q}_{\rm flasher}(\theta) = \mathcal{Q}_{\rm flasher}(0,0)\ f(\theta). \tag{29}$$

The factor $f(\theta)$ has been measured for a single LED at TurLab in the past. The details of the measurement are provided in [26] and are shown in black in Fig. 11. A second measurement has been performed in open-air employing the full flasher system.

Table 1
List of the campaigns performed with the *Torino UV flasher*.

Date dd/mm/yyyy	time ISS (CEST)	Place	Height (m)	Weather	Moon Phase	Session n.
04/05/2021	02:44	Piana di Castelluccio (Umbria)	1550	Excellent	45%	40
07/05/2021	02:00	Passo della Raticosa (Toscana)	970	Partly cloudy	20%	41
06/11/2021	23:30	Piana di Castelluccio (Umbria)	1550	Rainy	4%	45
25/10/2022	06:06	Colle di Tenda (Piemonte)	1870	Good weather/Sunrise [−21°;−19°]	0%	69
26/10/2022	05:19	Volterra (Toscana)	530	Good weather/Sunrise [−28°;−24°]	2%	70
30/10/2022	03:45	Sant'Antimo Abbey (Toscana)	320	Excellent	32%	71
17/01/2023	01:03	Caricatori (Piemonte)	1050	Excellent	27%	76
16/05/2023	02:55	Usseglio (Piemonte)	1260	Excellent/lightning in nearby area	12%	83
23/05/2023	00:28	Pian della Regina (Piemonte)	1770	Clear and cloudy patches	6%	84

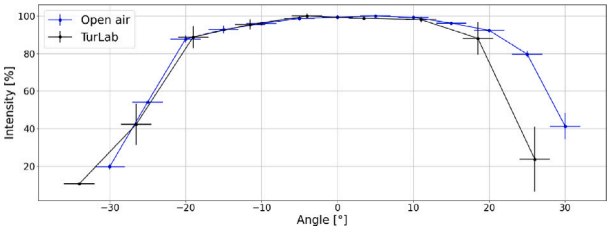

Fig. 11. The function $f(\theta)$ obtained as the intensity measured at different values of the angle between the lens optical axes and the detector. **Black:** results obtained at TurLab using a single LED (adapted from [26]). **Blue:** results obtained in open-air condition using the full flasher system.

The light emission is almost constant up to $\sim \pm 10°$, then it slowly decreases up to $\sim \pm 20°$ when it finally starts dropping off quickly. The difference between two curves is below 1% until $\pm 15°$, being appreciably different only for a small fraction of the most external pixels. In the rest of the paper only the result of the blue curve will be considered, given that it is obtain for a complete flasher system, not for only a single LED.

7. The acquisition campaigns

Between May 2021 and November 2023, 9 flasher campaigns were attempted with the *INFN Turin UV flasher*. Dates and conditions are reported in Table 1. Sessions 40 and 71 provided good data which are used in this analysis to derive Mini-EUSO end-to-end calibration. Sessions 41 and 45 were not successful due to the adverse climatic conditions (clouds and rain) while in Session 69 and 70 the Sun was already illuminating the ISS and the atmosphere below, therefore, Mini-EUSO was not operational at the time of flying over the flasher location. The data of Sessions 76, 83 and 84 have not been downloaded yet to ground, therefore, no information can be derived up to now. The rate of success is not surprising. In the JEM-EUSO case it was assumed about one good passage per station during the two weeks of low moon phase. It is reasonable to assume, even though part of the data is on the ISS, that the *INFN Turin UV flasher* was operated successfully 3–4 times in the 50 sessions between Sessions 40 and 90, which is in line with expectations.

7.1. The first attempt: Session 40

An example of data acquisition is shown in Fig. 12 which refers to the observation of the *INFN Turin UV flasher* during the passage over Piana di Castelluccio on Session 40 (May 4th 2021). The red rectangular box indicates the propagation of the flashing signal all along the FoV. Unfortunately, the flasher was detected in the last column of pixels of one MAPMT, complicating the extraction of the signal due to the presence of a large gap (~1.3 pixels) between two adjacent MAPMTs, which considerably increases the uncertainty. The expected flasher pattern (see Fig. 6 for comparison) clearly allows to

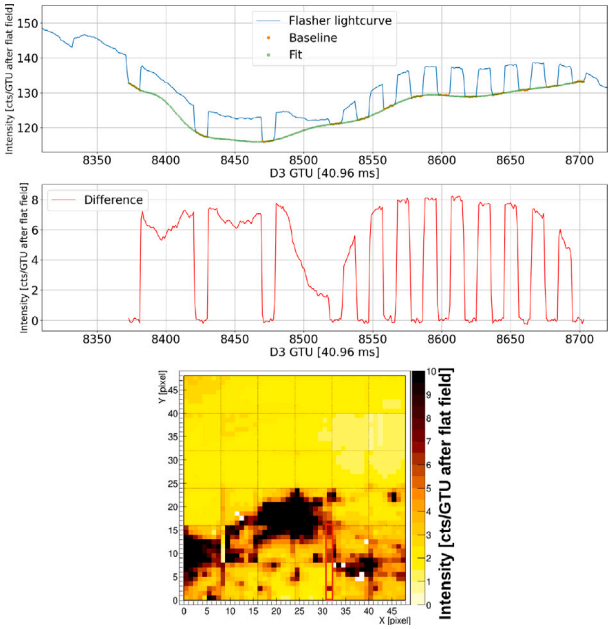

Fig. 12. Top: Lightcurve of the flasher LED photons detected by Mini-EUSO on the ISS during session 40 without (top) and with (bottom) subtraction of the background indicated by the green line. The flasher signal is clearly visible above the background, reaching up to 8 counts/GTU. The decay around GTU 8500 is due to the flasher crossing vertically the separation between two MAPMTs, causing some light to be lost in the gap. **Bottom:** Image of a frame of the data acquisition in D3. The red box indicates the pixels illuminated by the flasher during the evolution of the event.

associate the blinking signal with the observation of the flasher. Given the huge uncertainty caused by the light lost in the gap between two MAPMTs, the results obtained by the analysis of this session will not be discussed in detail here but they are reported in [26]. For the moment we will instead focus on the results obtained on Session 71 (October 30th 2022) during the flasher campaign performed at the location of Sant'Antimo Abbey (Tuscany, Italy).

7.2. Choice of the location

Immediately after the first observation on May 4th 2021, briefly mentioned above, we soon realized the importance of choosing a location not only inside the Mini-EUSO FoV, but also as far as possible from the MAPMT borders. Maps with the foreseen position of the ISS (and the Mini-EUSO FoV) for different ISS attitude values have been produced, an example is shown in Fig. 13.

The flasher location is then chosen once a place accessible by car, far away from major (and smaller, if possible) light sources, and close to the center of a column of MAPMTs for all the possible ISS attitude values, is found. We also monitor the weather conditions, to avoid ending up in a location where the presence of clouds or fog reduces the amount of light reaching the ISS by an unknown and uncontrolled

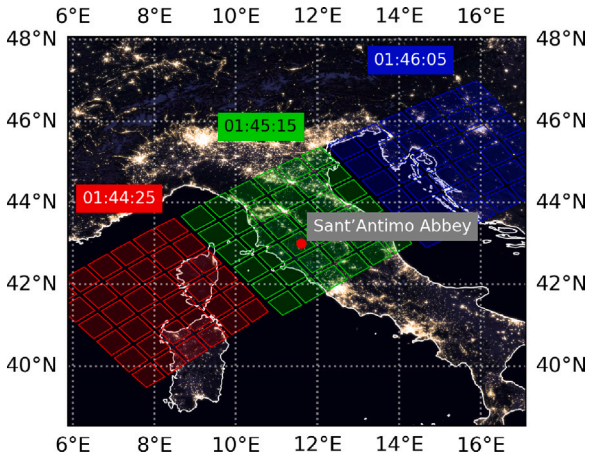

Fig. 13. Foreseen FoV of the Mini-EUSO telescope superimposed to the geographical map for the passage over Sant'Antimo Abbey, on October 30th 2022. It is possible to appreciate the dimension of the gaps between two MAPMTs. The background picture is taken from the Black Marble 2016 dataset available at https://visibleearth.nasa.gov/images/144898/earth-at-night-black-marble-2016-color-maps.

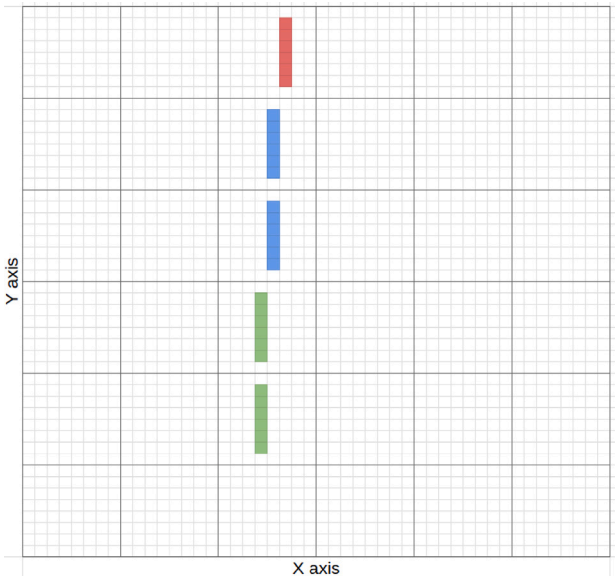

Fig. 14. Schematic view of the 2304 pixels that make up the Mini-EUSO PDM. The colored pixels represent the pixels considered in the analysis. The pixels close to the border of a MAPMT and the pixels of the bottom MAPMT, that suffer from light leakage, have been excluded from the analysis. The three different colors indicate the column of pixels with the maximum of the flasher signal, x = 19 in green, x = 20 in blue, x = 21 in red. The same color palette is used in other plots.

amount. Following these criteria, the flasher location in Session 71 was chosen to be next to the Sant'Antimo Abbey (Lat: 43.000642°, Lon: 11.517336°), exactly at the center of a column of MAPMTs. The chosen location is close to a series of very small villages but far away from any major or medium city, in an environment dark enough to perform the measurement without any additional problems. The weather conditions on that night were perfect, without fog or clouds in a large area around the chosen location, as discussed in Appendix B. Once on the chosen spot, the flasher system has been switched on a couple of minutes before the forseen passage of the ISS, and switched off after 5 min of constant flashing. In the following Sections, the results obtained through the analysis of this field measurement are presented.

8. Absolute pixel calibration method

We now apply the method presented in Section 4.1 to determine the efficiency η_i defined in Eq. (18) for 30 pixels which observed the *INFN Turin UV flasher* during the campaign of October 30th, 2022, described in Section 7.

As the ISS passes over position $\vec{r}_0$ where the flasher is installed, the source enters the FoV of Mini-EUSO on one side of the PDM (the bottom side on Fig. 14) and moves through it almost parallel to the columns of pixels, depending on the yaw of the ISS at the time of measurement. During the campaign, the flasher crossed 3 pixels in the X-axis (from column x = 19 to column x = 21) while crossing the entire PDM (48 pixels) in the Y direction. Fig. 14 shows the position of the pixels considered in the analysis. As can be seen, the pixels near the edge of a MAPMT are excluded from the analysis, being too close to the gap between two MAPMTs. We also excluded the bottom MAPMT because of a light leak during the session (due to a defective latch attaching the Mini-EUSO telescope to the window).

To derive the efficiency of these 30 pixels, we determine the two quantities of Eq. (23), firstly the numerator $N_i^{(5\times5)}$ from the measurements, and then the denominator $N_i^{(\text{window})}$.

9. Photon counts from the *INFN Turin UV flasher*

In this first step, we determine the value of $N_i^{(5\times5)}$ defined in Eq. (21), where the index i corresponds successively to each of the 30 pixels under study.

The procedure is demonstrated in Fig. 15 in the case of pixel ($x = 20, y = 29$). On the top panel, we show in blue the light curve of this pixel, i.e. the photon counts as a function of time (expressed in D3 GTU, i.e. in units of 40.96 ms since the switch on of the instrument in the current orbit). The flasher was on from GTU = 16 534 to GTU = 16 642. As can be seen, the photon counts are increasing and later decreasing, as the flasher enters and leaves the nominal FoV of the pixel.

On the plot, we also show in orange the light curve of the previous pixel (the one below in Fig. 14), which saw the flasher before the pixel of interest, as well as the light curve of the following one (in green), which saw the flasher subsequently. As can be seen, the previous (following) pixel still (already) receives light from the flasher when it is in the middle of the current pixel. This is a result of the imperfect PSF, which extends beyond a single pixel. This is also the reason why we need to sum the signal over a larger area on the focal surface.

These lightcurves include both the signal from the flasher and some background light. We thus first remove this background, estimated in each GTU by a third-degree polynomial fit. Only the GTUs for which the flasher was off, before and after the switch on, were used in the fit (in the plot GTUs 16 524–16 532 and GTUs 16 644–16 652, between the black vertical lines). The resulting light curves are shown on the second panel.

To compute the quantity $N_i^{(5\times5)}$, we finally need to rescale the individual photon counts by the corresponding efficiency ratio, according to Eq. (21). The result is shown in the third panel of Fig. 15 for the four closest neighbors.

In the fourth panel, we show separately the contribution of the central pixel (in blue), the contribution of the 24 other pixels in the (5×5) box around it (in light red) and the contribution of the 16 pixels on the outer ring of the box (in purple), the evolution of the two quantities $N_i^{(3\times3)}$ (in black) and $N_i^{(5\times5)}$ (in red). In this particular example, the contribution of the main pixel appears to reach ~50% of the total at its maximum, while the (3×3) box collects roughly 90% of the signal inside the (5×5) box.

Importantly, the sum of the (rescaled) signal over the full (5×5) pixel box (namely $N_i^{(5\times5)}$) appears almost constant over the entire flash, which is a direct confirmation of the assumption made in the previous section that, while $\text{PSF}(\vec{r}_0 \to j)$ strongly depends on the position of the

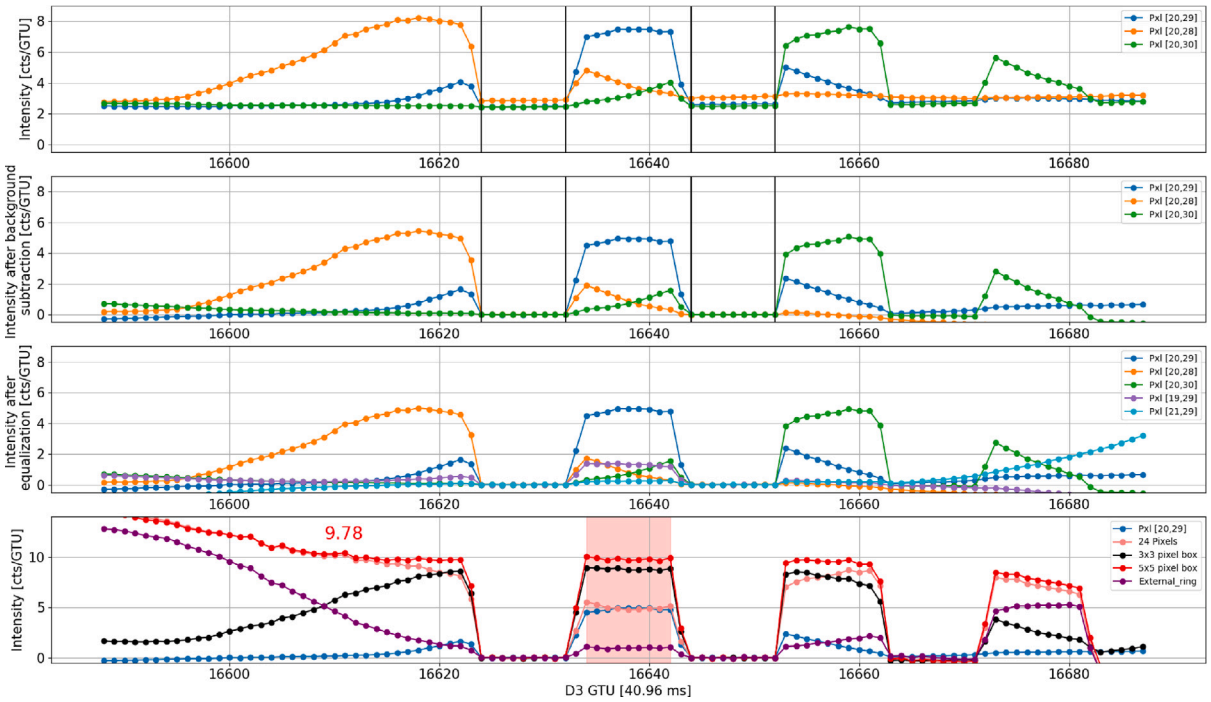

Fig. 15. Analysis of the pixel [20,29]. In the plots the black vertical lines indicate the GTUs when the flasher switches on and off, the red background indicates the GTUs when the flasher is on. **Top:** Lightcurve of the Central pixel (blue), and the pixels below (orange) and above (green) it. The flasher signal appears firstly in the bottom pixel, eventually moving towards the top. **Middle Top:** The same lightcurves as before, after the background subtraction. **Middle Bottom:** the lightcurves of the central pixel and of its four immediate neighbors, rescaled through the factor expressed in Eq. (20). **Bottom:** lightcurve of (5×5) (red) and (3×3) (black) box, of the central pixel (blue), the sum of the other 24 pixels (light red) and of the 16 most external pixels (purple). The red number indicates the average value of the counts in the (5×5) box when the flasher was on.

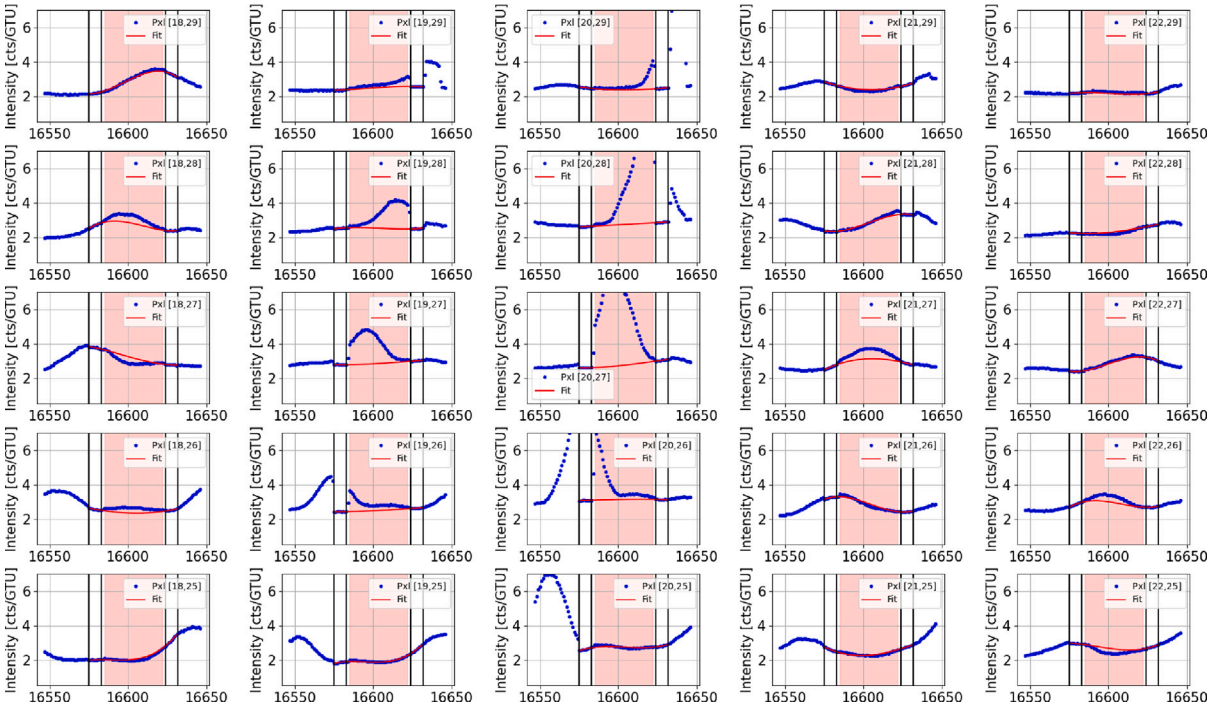

Fig. 16. Example of background estimation for a long pulse of the flasher. The 25 panels show the lightcurve (blue) and the estimated background (red) for the pixels belonging to the 5 × 5 pixel box centered around pixel [20,27]. The fit extrapolates the value of the background when the flasher is active (red background) based on the measured values when the flasher is off (between the black vertical lines). While the result is good in the vast majority of the cases, and in particular for the 3 × 3 internal box, there are a few pixels in which the background is clearly underestimated (pixels [18,28] and [22,26]) or overestimated (pixels [18,27] or [22,25]).

light source ($\vec{r}_0$) within a given pixel, this is not the case for the sum of these quantities over a (5×5) pixel box which is simply proportional to $N_i^{(5\times5)}$ according to Eq. (21). It also appears that summing only over a (3×3) box around the main pixel would underestimate the total number

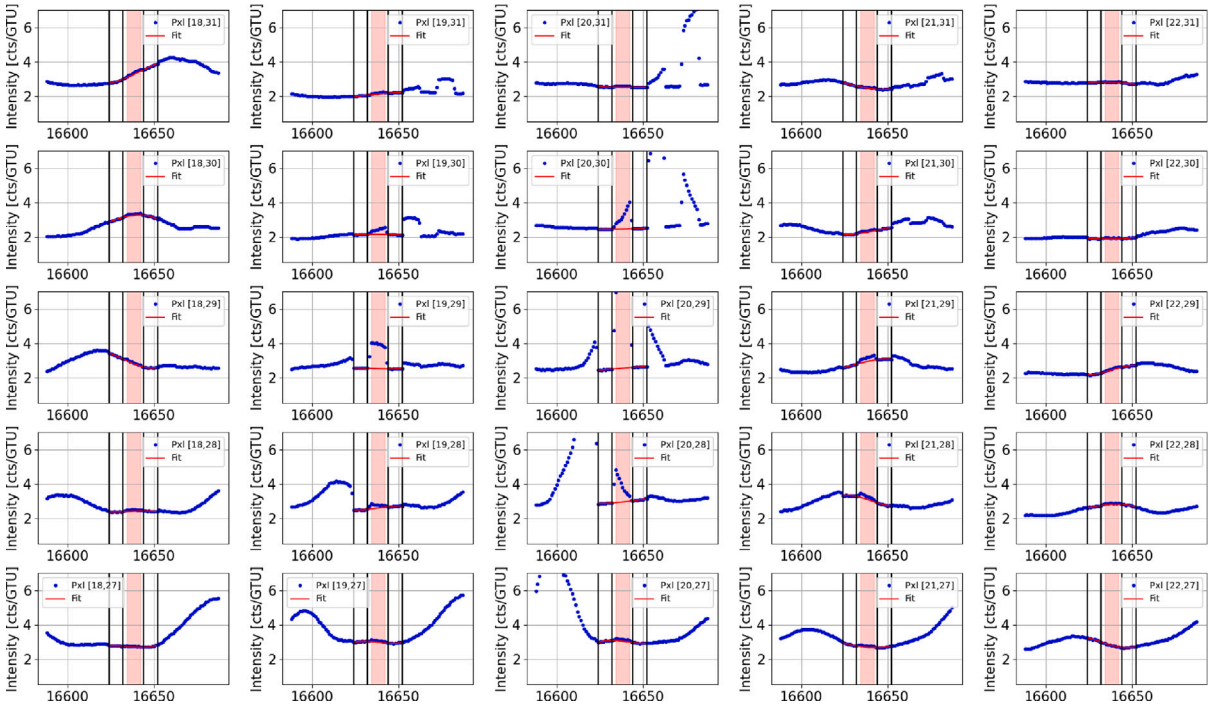

Fig. 17. Example of background estimation for a short pulse of the flasher. As opposed to the example shown in Fig. 16, in the case of short pulses the background estimation procedure gives good results over the whole (5×5) pixel box.

of photons received from the flasher by ∼10% (somewhat dependent on the pixel position in the PDM).

Ideally, the same procedure would be applied to all the other 29 pixels considered in the analysis. Unfortunately, this is not possible for two distinct reasons. Firstly, 10 out of the 30 analyzed pixels are only one pixel away from the gap between two MAPMTs. As a consequence, the procedure mentioned above cannot be applied since part of the light that is usually focused on the external ring is instead lost in the gap.

Secondly, it is very difficult to correctly model the background when the pixels observe the long flasher pulses (lasting ∼1.6 s, corresponding to ∼40 D3 GTUs). This problem is exemplified in Fig. 16 where are shown the lightcurves of the 25 pixels belonging to the 5 × 5 box centered around pixel [20,27] (in blue) along with the background estimation (in red). As previously mentioned, the background is modeled through a 3-degree polynomial fit using only the values measured by each pixel when the flasher is off (indicated in the plot by the black vertical lines). In some cases the fit is not able to correctly follow the evolution of the background, especially in the presence of other ground sources (which appear as ∼40 GTUs large peaks repeating in all the pixels of the same column, with a time delay of ∼25 GTUs). This effect is more evident for the pixels belonging to the external ring, both because the flasher signal is less intense, and because some ground sources are always present (consider for example the peak that is present in pixel [18,26] around GTU 16 550, in pixel [18,27] at GTU 16 575, in pixel [18,28] at GTU 16 600 and in pixel [18,29] at GTU 16 625). It is worth pointing out that the same ground source is always visible in the leftmost column of 5 × 5 box for all the analyzed pixels, given that they are observing the same position around the flasher location at different times. The difficulty of the background modeling is therefore a problem appearing for all the analyzed pixels that observe a long pulse of the flasher.

The background subtraction is in fact a much more accurate process in the cases of short pulses when only ∼10 GTUs have to be modeled, as shown in Fig. 17. As a consequence, the value of $N_i^{(5\times5)}$ is much more accurate for the pixels observing short pulses than for the others. On the other hand, the result obtained considering only the (3×3) pixel box

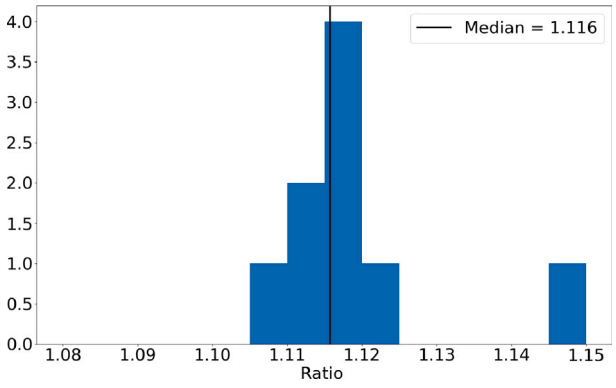

Fig. 18. Ratio between the values of $N_i^{(5\times5)}$ and $N_i^{(3\times3)}$ for the pixels observing the short pulses of the flasher.

(namely $N_i^{(3\times3)}$) is sufficiently accurate in all the cases, given that no major ground source is present in the area observed by the inner ring of pixels. In the next section a method to derive the value of $N_i^{(5\times5)}$ from $N_i^{(3\times3)}$ for all the 30 analyzed pixels will be presented. The use of this method will overcome the two problems mentioned earlier in this section (the impossibility of computing $N_i^{(5\times5)}$ for pixels close to the edge of MAPMTs and the difficulty of modeling the background for pixels observing long pulses).

9.1. *The* (3×3) *pixel box method*

To apply the new method, we start by computing the ratio

$$R_{(3\times3)}^{(5\times5)} = \frac{N_i^{(5\times5)}}{N_i^{(3\times3)}} \tag{30}$$

for the 9 pixels i observing short pulses that are at least two pixels away from the gap between MAPMTs. This ratio, shown in the form of a

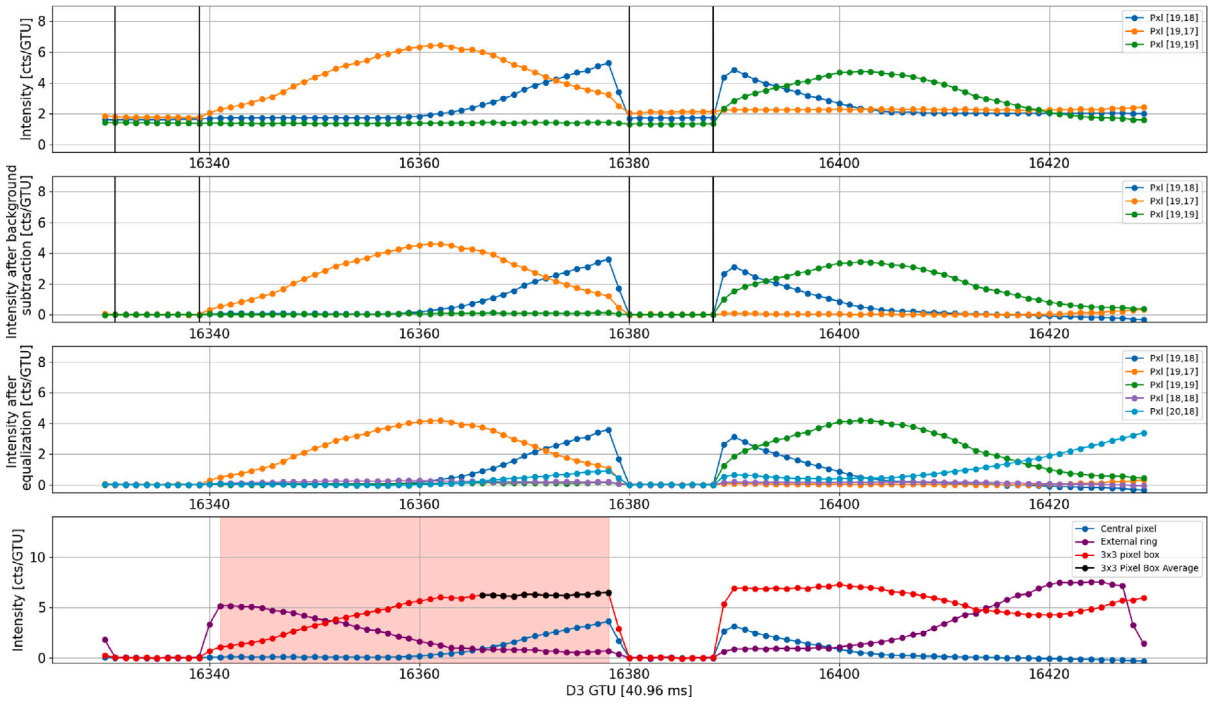

Fig. 19. Analysis of the pixel [19,18]. The first three panels show the same quantities presented in Fig. 15. **Bottom:** sum of the rescaled signal within the (3×3) pixel box (red), together with the lightcurve of the central pixel (blue), and the sum of the 16 most external pixels of the (5×5) pixel box (purple). The value of the signal is computed as the average over the black points, identified as the GTUs in which the flasher was on (red background) and the signal on the external ring (purple) is lower than the signal in the central pixel (blue).

histogram in Fig. 18, is fairly constant for all the 9 pixels, with a median value of $R^{(5\times5)}_{(3\times3)} = 1.116$ and a standard deviation of $\sigma_{R^{(5\times5)}_{(3\times3)}} = 0.01$. The value of this ratio is representative for all the pixels for which stands the hypothesis of a locally symmetric PSF, and therefore also for all the 30 considered pixels. We proceed to evaluate $N_i^{(5\times5)}$ for the 30 analyzed pixels as

$$N_i^{(5\times5)} = N_i^{(3\times3)} \times R^{(5\times5)}_{(3\times3)} \tag{31}$$

This has the double advantage to increase the number of analyzed pixels to 30, and to reduce significantly the error introduced by the background subtraction, which we can estimate to be 1% for the short pulses and 5% for the long pulses. The experimental procedure to obtain the values for $N_i^{(3\times3)}$ is similar to the one presented before, and exemplified in Fig. 19 where the first three panels show the same procedure described for Fig. 15. $N_i^{(3\times3)}$ (shown in red in the fourth panel) is not always constant over the period when the flasher is on (light red background) but it increases (decreases) while the flasher is entering (exiting) the nominal FoV of the 9 pixels. It is however constant when the flasher is well within the considered box, which we define as the GTUs when the sum of the signal observed by the 16 pixels of the external ring of the (5×5) pixel box (purple) is lower than the signal observed by the central pixel (blue). These GTUs are indicated in the fourth panel by the black points, and the average of $N_i^{(3\times3)}$ over this period is used to compute $N_i^{(5\times5)}$ through Eq. (31). The result is shown by the black curve in Fig. 20.

10. Determination of the number of photons reaching the ISS window $N_i^{(\text{window})}$

The denominator Eq. (22), which represents the number of photons produced by the flasher and reaching the ISS window, namely

$$N_i^{(\text{window})} = \mathcal{Q}_{\text{flasher}}\, f(\Theta_i)\, \Delta t_{\text{GTU}}\, \Omega_i\, T_i^{(\text{atm})}, \tag{32}$$

is the final element necessary to obtain the end-to-end efficiency. It has to be computed for the 30 values of the angle Θ_i corresponding to the viewing angle of the 30 analyzed pixels. $\mathcal{Q}_{\text{flasher}}$ is obtained through the measurements presented in Section 6 and its numerical value is expressed in Eq. (26). $f(\Theta_i)$ is also measured, as explained in Section 6.4, its value is shown in Fig. 11 as a function of the angle θ. Ω_i, directly proportional to the factor $\cos^3\Theta_i$, is expressed in Eq. (4). The only missing element is the atmospheric absorption $T_i^{(\text{atm})}$, estimated in the next Section.

10.1. Atmospheric transmittance

We can parameterize the atmospheric transmittance in the direction observed by pixel i, $T_i^{(\text{atm})}$ as

$$T_i^{(\text{atm})} = T_{0^\circ}^{(\text{atm})}\; L_i^{(\text{atm})}, \tag{33}$$

namely the product of a constant (and error-less) factor $T_{0^\circ}^{(\text{atm})}$ that measures the transmittance in the zenith direction, and a function $L_i^{(\text{atm})}$, defined as

$$L_i^{(\text{atm})} = \frac{T_{\Theta_i}^{(\text{atm})}}{T_{0^\circ}^{(\text{atm})}}, \tag{34}$$

where Θ_i represents the value of the viewing angles of the 30 pixels considered in the analysis. $L_i^{(\text{atm})}$ gives the angular dependencies of the atmospheric transmittance. As opposed to $T_{0^\circ}^{(\text{atm})}$, which strongly depends on the specific atmospheric condition in a given time and place, $L_i^{(\text{atm})}$ is almost constant in every condition.

Both the quantities, $T_{0^\circ}^{(\text{atm})}$ and $L_i^{(\text{atm})}$ was calculated using the libRadtran package [29,30] for a ground-based flasher signal. An atmospheric model, assuming clear sky conditions, was applied for the location and time of observation. Local aerosol conditions were modeled using Aerosol Optical Depth (AOD) parameter measured by MODIS satellite spectrometer [31]. AOD is a measure of the extinction of the solar beam by dust and haze. It quantifies how much sunlight is prevented from reaching the ground by aerosol particles in the atmosphere. The AOD value of 0.043 measured by MODIS at 550 nm (default published wavelength) was used as one of the parameters

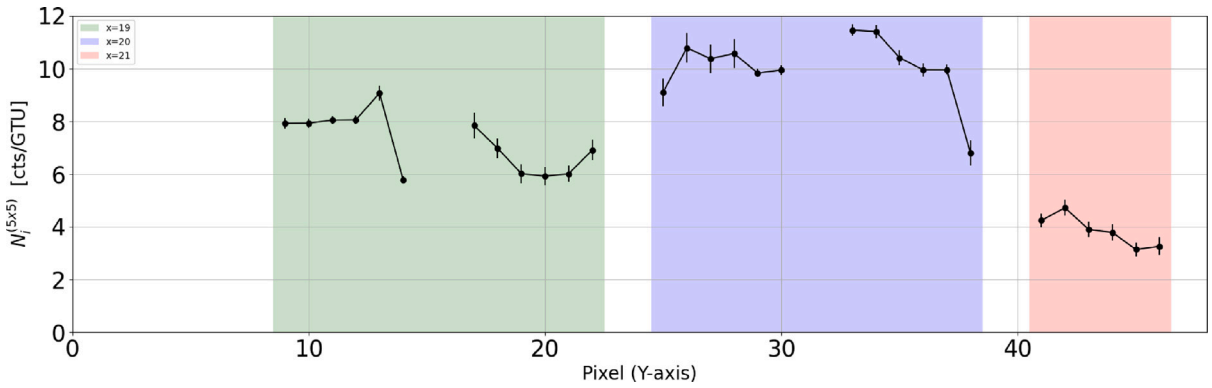

Fig. 20. Equivalent counts produced by the flasher and focused in a (5×5) box centered around the analyzed pixels. The values are obtained through Eq. (31), starting from the counts observed in a (3×3) box. The colors in the background indicate the column of pixels with the maximum of the flasher signal, x = 19 in green, x = 20 in blue, x = 21 in red. The horizontal axis indicates the other coordinate. The points connected by a solid line refer to pixels belonging to the same MAPMT.

in the libRadtran calculations. AOD measurements over land have an uncertainty of 0.05 + 0.2 · AOD [31] what gives acceptable values of AOD in the range between 0 and 0.102, affecting the calculated transmittance accuracy and giving the error visible in Fig. 21. The uncertainty of the atmospheric transmission is not always linear with the AOD parameter. Additional parameters used in the LibRadtran computation are the AFGL [Air Force Geophysics Laboratory] midlatitude winter as the atmosphere model and a value of 360 Dobson units[2] for the ozone layer.

Calculations with libRadtran were made for various observation angles in 0.1-degree steps to address different Mini-EUSO detector pixels at varying optical axis distances. Fig. 21 illustrates the atmospheric transmittance as analyzed with libRadtran software. The upper panel presents transmittance as a function of wavelengths for nadir observations performed during the flasher campaign, highlighting the uncertainty range. The red marker pinpoints the efficiency peak of the LED flasher (400 nm) resulting in a value of $T_{0°}^{(\mathrm{atm})}\ L_{0°}^{(\mathrm{atm})} = (66.3^{+4.4}_{-5.6})\%$. The lower panel details the transmittance variations at 400 nm against the off-axis observation angles, showcasing the distinction between nadir and the maximum considered off-axis angle of 20.5°. From this is it possible to obtain the values of $L_i^{(\mathrm{atm})}$ and their uncertainties for the 30 analyzed pixels. The calculated transmittance includes Rayleigh scattering, the influence of ozone, and scattering on aerosols. The upper value for a 0° angle, reaching 70%, corresponds practically to Rayleigh scattering only (with the boundary condition of AOD = 0.0, meaning the absence of aerosols). Due to the relatively narrow emission angle of the UV diode and the geometry of the measurement setup, the light diffused in the atmosphere was neglected, considering only the direct beam.

10.2. Photons at the ISS window

Fig. 22 shows the numerical values of the viewing angles Θ_i and of all the factors depending on them, namely $L_i^{(\mathrm{atm})}$, $f(\Theta_i)$ and $\cos^3\Theta_i$, for the 30 pixels considered in the analysis. The numerical values of the angles Θ_i are obtained taking into account the value of the ISS attitude, namely the yaw pitch and roll angles. The product of $L_i^{(\mathrm{atm})}$, $f(\Theta_i)$ and $\cos^3\Theta_i$ appears in the definition of $N_i^{(\mathrm{window})}$ in Eq. (32), namely the number of photons reaching the ISS window when the flasher is viewed by one of the analyzed pixels. This value can now be computed for the 30 different pixels. The result is shown in Fig. 23.

[2] The Dobson unit is a unit of measurement of the amount of a trace gas in a vertical column through the Earth's atmosphere. An ozone layer of 360 Dobson units is equivalent to a pure ozone layer of 3.6 mm thickness at standard temperature and pressure.

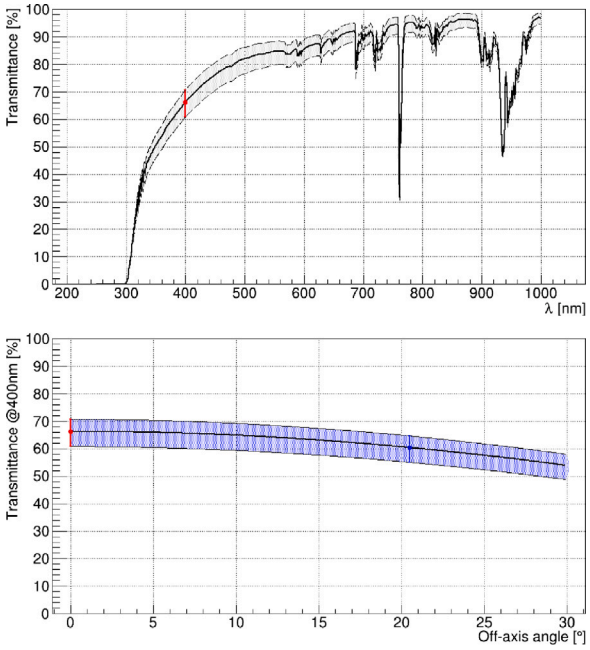

Fig. 21. Atmospheric transmittance calculated using the libRadtran software. **Top:** transmittance as a function of wavelength for nadir observations under atmospheric conditions prevalent during the flasher campaign. The gray area represents the uncertainty region stemming from the measured AOD parameter's uncertainty. The red point, marked with error bars, corresponds to the 400 nm wavelength — the peak efficiency wavelength of the LED flasher. **Bottom:** transmittance at 400 nm as a function of the off-axis observation angle, namely $T_{0°}^{(\mathrm{atm})} \times L_i^{(\mathrm{atm})}$. The blue area represents the uncertainty. The red point is associated with observations by the detector's central pixels (nadir), and the blue point represents an off-axis angle of 20.5° — the pixel with the maximum off-axis angle considered in this analysis.

11. Efficiency measurements

11.1. Efficiency of the analyzed pixels

From the values of $N_i^{(5\times5)}$ and $N_i^{(\mathrm{window})}$, obtained in Sections 9 and 10 respectively, we can finally compute the efficiency η_i for the 30 analyzed pixels, through the formula expressed in Eq. (23). The result is shown in Fig. 24. The efficiency is reported with two different types of error bars, one representing the statistical uncertainties of the measurement, given by the uncertainties on the angle Θ_i, the variability of the detected photon counts and the background subtraction procedure, the other one coming from the variability of the flasher emissivity, as highlighted in Section 6, which represents a systematic uncertainty.

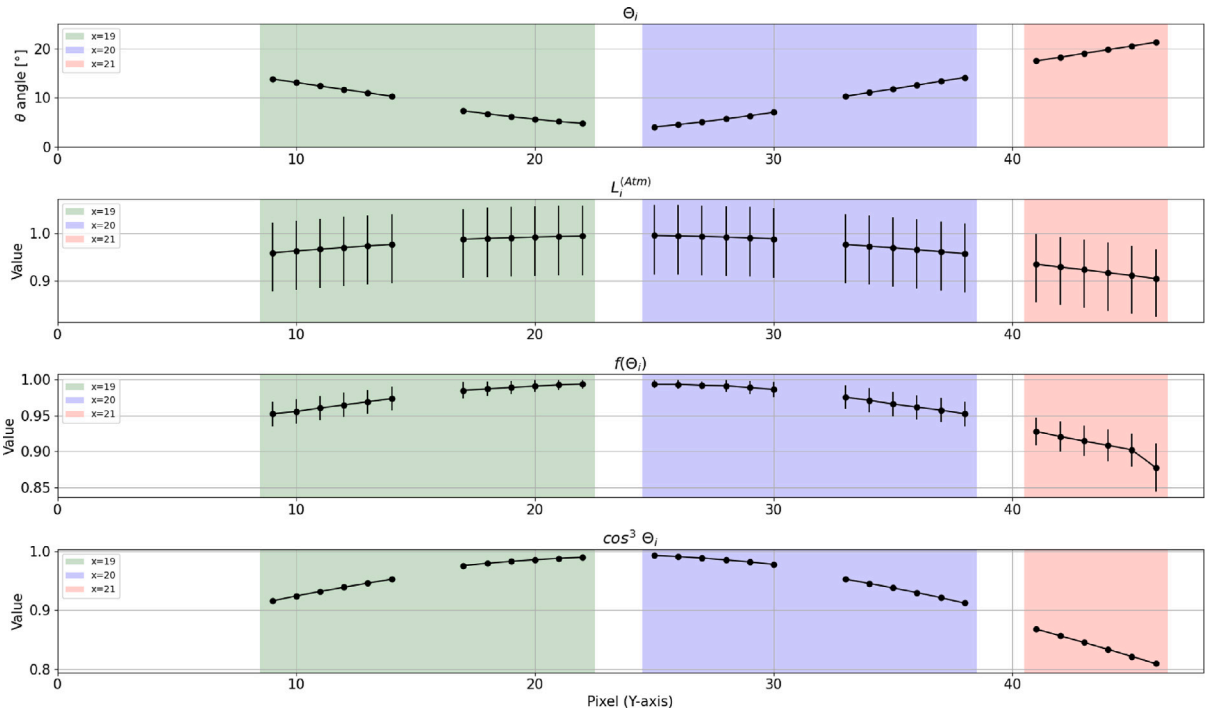

Fig. 22. Top: angle Θ_i from the nadir observed by the pixels considered in the analysis. The values take into account the ISS attitude (the yaw, pitch, and raw angles). **Middle Top:** Numerical values of the correction factor $L_i^{(atm)}$ expressed in Eq. (34), that takes into account a larger atmospheric absorption due to the longer path traveled by the photons to reach the ISS window. 100% correspond to the flasher at $\theta = 0$. The asymmetric error bars come from the results obtained through libRadTran software shown in Fig. 21. **Middle Bottom:** Values of the curve in Fig. 11 for the angles of the considered pixels. It compensates for the non-uniformity of the lens in front of each UV LED. **Bottom:** Value of the $\cos^3\theta$ factor for the different values of Θ_i.

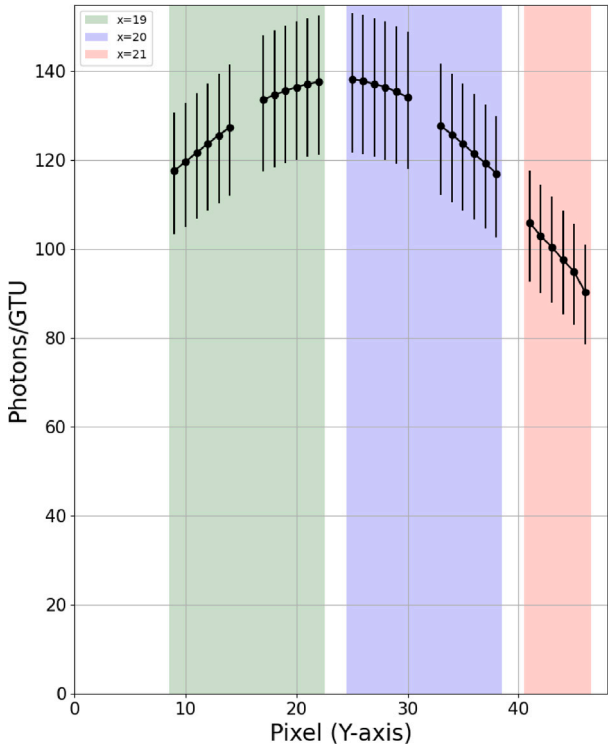

Fig. 23. Estimation of the number of photons per GTU produced by the *INFN Turin UV flasher* that reaches the window of the ISS when the flasher is seen by each of the analyzed pixels. The difference between the pixels is caused by the different angle factors shown in Fig. 22. The solid lines connect all the pixels belonging to the same MAPMTs.

As expected, the efficiency of the 30 pixels is not the same, ranging from a minimum of 3.3% for pixel [21,45], to a maximum of 9.1% for pixel [20,34]. The next step is to check whether the obtained values are compatible with one another using the known relative efficiency obtained in the form of flat field values.

11.2. Consistency check of the measured efficiencies

As shown in Appendix A.1, the flat field values represent a relative calibration factor that takes into account the difference in the absolute efficiency of the pixels, the different dimensions of the footprint on ground and the different viewing angles. The explicit parametrization of the flat field value of pixel i is derived in Appendix A and expressed in Eq. (A.4) that we report here for convenience

$$\mathrm{FF}_i = \frac{S_i \; L_i^{(\mathrm{Atm})} \; \cos^3\theta_i \; \eta_i}{\langle S_k \; L_k^{(\mathrm{atm})} \; \cos^3\theta_k \; \eta_k \rangle_{k\in RPs}} \,, \tag{35}$$

As explained in the Appendix, the denominator has to be intended as an average over a subset of pixels previously identified as the most stable from one orbit to another. This subset is usually referred to as Representative Pixels (or *RPs*). The values of S_i and θ_i, importantly, take into account the attitude of the ISS (namely the altitude and the yaw, pitch, and roll angles) that can vary between orbits and sessions (and only marginally within a single orbit).

All the quantities appearing in the numerator are known for the 30 analyzed pixels, so it is possible to use their flat field values FF_i to compare the measured efficiency. We can divide the measured efficiency η_i by a rescaling factor R_i^{FF} defined as:

$$R_i^{FF} = \frac{\mathrm{FF}_i}{\frac{S_i}{\langle S\rangle} \; L_i^{(\mathrm{atm})} \; \cos^3\theta_i} = \frac{\eta_i}{\langle \frac{S_k}{\langle S\rangle} \; L_k^{(\mathrm{atm})} \; \cos^3\theta_k \; \eta_k \rangle_{k\in RPs}} \tag{36}$$

where the first expression has to be intended as the operational procedure to obtain the values of R_i^{FF} and the second as its parametrization. To make it easier to handle, we made this quantity dimensionless, by

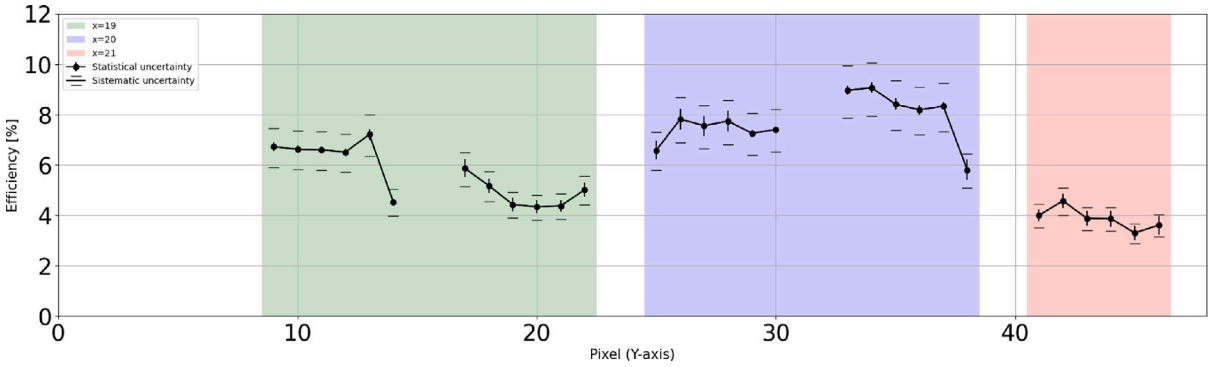

Fig. 24. Efficiency η_i measured for the pixels considered in the analysis, obtained through the formula expressed in Eq. (23). The points connected by a solid line refer to pixels belonging to the same MAPMT.

dividing the area of the pixel footprint on ground S_i by the typical value of the footprint of a pixel $\langle S \rangle$ considering the typical ISS attitude (altitude of 420 km, yaw, pitch and roll angles equal to 0) that result in $\langle S \rangle = 34.6$ km^2. Using the latter expression, we obtain

$$\frac{\eta_i}{R_i^{FF}} = \langle \frac{S_k}{\langle S \rangle} \, L_k^{(\mathrm{atm})} \, \cos^3 \theta_k \, \eta_k \rangle_{k \in RPs} \equiv H_{RPs} \tag{37}$$

which is a constant (and dimensionless) quantity, being an average over the specific subset of RPs that we chose to compute the flat field. We call this quantity H_{RPs} indicating that its numerical value should only depend on the choice of the representative pixels. It is worth noting, however, that both S_k and θ_k depend on the ISS attitude and, as such, change from session to session. H_{RPs} can be seen as a measurement of the average "effective efficiency" of the RPs, being an average of the efficiency multiplied by the factors that depend on the specific viewing angles of the *RPs*. Currently, two different subsets of RPs are available: the first one (that we call Representative Pixels: Set or 1 *RPs-S1*) has been used to obtain the flat field value in all the published Mini-EUSO work so far, such as [19]. Once a larger dataset has been available, a second subset of *RPs* (*RPs-S2*) has been identified. Both are used in the following part of the paper.

We can now use Eq. (37) and compute the value of H_{RPs} for the 30 measurements of η_i shown in Fig. 24. The results, shown in Fig. 25 for both the $RPs-S1$ and $RPs-S2$, can be interpreted as 30 independent measurements of the same quantity H_{RPs-S1} or H_{RPs-S2}. We here reiterate that the difference between the two is only due to the different choice of the Representative Pixels which is, ultimately, only a rescaling factor for the flat field. The choice of the RPs might influence the comparison between different orbits and sessions, but it does not affect measurements obtained within the same orbit.

As expected, the spread of the result is quite small, with a standard deviation of 11.3% and only a few pixels presenting a measured value sensibly different from the average. This result illustrates the precision of the calibration procedure, the flat field derivation, and the parametrization presented in this work. The horizontal red [blue] line indicates the average of the data points, corresponding to

$$H_{RPs-S1} = (6.1 \pm 0.13 \ \pm 0.7)\%$$

$$[H_{RPs-S2} = (10.0 \pm 0.2 \ \pm 1.1)\%],$$

where 0.13 [0.2] is the standard error of the mean and 0.7 [1.1] is the systematic uncertainty on the flasher emissivity. We can consider the quantity $\frac{0.13}{6.1} \sim \frac{0.2}{10.0} \simeq 2\%$ as an estimation of the statistical uncertainty of the calibration process. The systematic uncertainty is mainly due to the calibration of the flasher itself and the uncertainty of the atmospheric transmittance, resulting in a value close to 11%.

11.3. Derived efficiency of the other pixels

The results obtained so far are a direct measurement of the efficiency η_i of the 30 analyzed pixels and the parameter H_{RPs}. We can now invert the procedure, and instead of using the flat field values of the pixels to obtain an experimental value of H_{RPs}, we can rely on the obtained average value of H_{RPs} and on the flat field values to obtain the efficiency η_i for all the other pixels of the Mini-EUSO detector for this particular orbit. The efficiency obtained in this way is no longer a direct measurement but is a mere rescaling of the measured relative efficiency through the flat field values. The flat field values themselves change from orbit to orbit and from session to session, which implies that also the efficiency obtained in this way will change accordingly. With that in mind, it is possible to derive the efficiency of any pixel j through the formula:

$$\frac{\eta_i}{R_i^{FF}} = H_{RPs} = \frac{\eta_j}{R_j^{FF}} \tag{38}$$

from which

$$\eta_j = H_{RPs} \times R_j^{FF} \tag{39}$$

It is worth noticing that the value of η_j does not depend on the choice of the RPs, given that the value of H_{RPs} and the flat field changes accordingly.

The result of Eq. (39) is shown in Fig. 26. 83 pixels (3.6% of the total) with unusually high or low flat field values have been excluded from the plots. 64 of them belong to a MAPMT which suffers from a problem of bit-shift that roughly doubles the observed photon counts (and the flat field values). Another cluster of removed pixels presents higher counts than usual because of the light leakage due to a broken latch mentioned in Section 8. The rest belong to a few border pixels, that we know are intrinsically different from the others, being larger in size and sometimes presenting the problem of double-counting of the photo-electrons, the process in which a secondary electron generated in the cascade inside the photo-multiplier initiates a secondary cascade, producing therefore two photon counts instead of one.

As expected, the efficiency distribution does not peak around a very specific value but is instead quite large. The average is 7.3% and more than 50% of the pixels have an efficiency higher than 6% and lower than 11%. This large spread is due to several reasons, among which are the uncertainties of the flat field procedure and the sub-optimal "DAC values" used for several pixels. The so-called DAC value indicates the voltage threshold at the ASIC level used to identify a photo-electron. Typically, this threshold is set to a value corresponding to the valley between the typical noise of the ASIC (the "pedestal") and the photo-electron peaks. When dealing with low-gain pixels, however, the separation between the photo-electron peak and the pedestal might be very small. That is often the case for Mini-EUSO pixels, since Mini-EUSO is operated at a high-voltage slightly lower than the optimal one (950 V instead of 1000 V), to prevent damage to the MAPMT and to

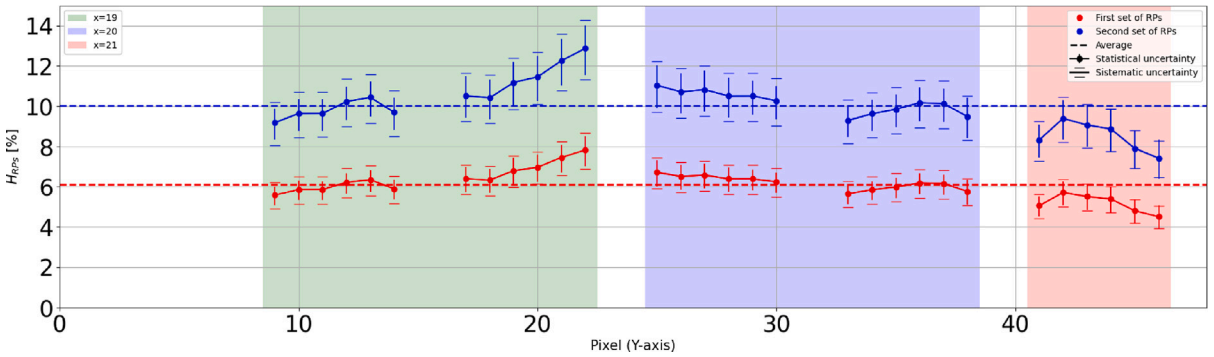

Fig. 25. Value of the quantity H_{RP_S} defined in Eq. (37). The points connected by a solid line refer to pixels belonging to the same MAPMT. **Red:** Value of H_{RP_S-S1}, obtained using the first set of Representative Pixels. **Blue:** Value of H_{RP_S-S2}, obtained with the second set of Representative Pixels.

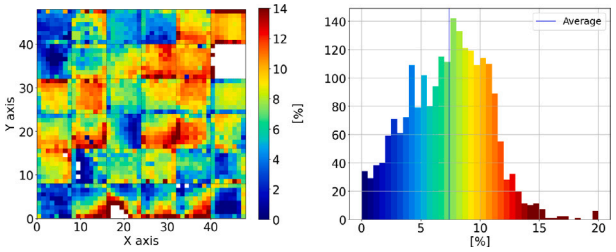

Fig. 26. Efficiency of the entire PDM derived through Eq. (39). 83 pixels with unusual high or low flat field values have been removed from the plot, see the text for the details. **Left:** Map of the efficiency. **Right:** histogram of the values. The color scale (in percent) is common to the two panels. The average value is 7.3%. More than 50% of the pixels have an efficiency higher than 6% and lower than 11%.

increase their life expectancy. In the near future we plan to mitigate this problem by performing specific measurements to determine the optimal DAC value for each pixel.

12. Conclusions and perspectives

An in-flight end-to-end calibration procedure for the Mini-EUSO detector has been developed. This is part of the realization of the Global Light System of a space-based observatory for UHECRs aiming at validating the triggering efficiency, the accuracy of intrinsic luminosity measurements, and the reconstructed pointing direction accuracy. Several campaigns have been operated using the flashing systems developed at INFN Rome, APC France and INFN Turin.

In this paper we first introduce a parametrization of the Mini-EUSO photon counts in different specific conditions in terms of specific quantities. We then use this parametrization to derive an experimental procedure to obtain the end-to-end efficiency of the Mini-EUSO pixels that observed the *INFN Turin UV flasher* on ground. We mainly reported about the measurements performed on October 30th, 2022 and the flasher calibration performed in the laboratory by means of two absolutely calibrated photo-diodes.

We showed how it is possible to estimate the number of photons emitted from the flasher that eventually reach the ISS, based on the measurements performed in the laboratory. We developed a robust technique to obtain the number of photo-electrons produced by the flasher photons in several pixels along the focal plane. The ratio of these two quantities gives the best estimation of the absolute efficiency for 30 pixels of the Mini-EUSO telescope.

We showed that the measured efficiencies of the pixels agree with the previously known efficiency ratios expressed in the form of flat field values, within a factor of 11.3%. From that, the efficiency for all the 2304 pixels has been derived. The efficiency of the pixels results in being quite different from pixel to pixel, as expected, with an average of 7.3%. Several causes have been identified for the large spread of the efficiency, mainly the use of sub-optimal DAC values used for the PDM. This can be corrected, and specific measurements to obtain the optimal DAC values to be used will be scheduled soon.

The experimentally derived values are being currently used to provide absolute measurements of the detected UV intensity in order to evaluate the exposure and sensitivity to UHECRs by a large space-based experiment. Moreover, they will be used for all the other analyses related to the scientific exploitation of Mini-EUSO data. This measurement represents the first attempt at an end-to-end calibration of a space-based experiment for UHECRs using the fluorescence technique.

CRediT authorship contribution statement

M. Battisti: Writing – review & editing, Writing – original draft, Visualization, Validation, Software, Methodology, Formal analysis, Data curation, Conceptualization. **M. Bertaina:** Writing – original draft, Supervision, Methodology, Conceptualization. **E. Parizot:** Writing – original draft, Supervision, Methodology, Investigation, Funding acquisition, Formal analysis. **M. Abrate:** Validation, Investigation. **D. Barghini:** Writing – original draft, Validation, Supervision, Investigation. **A. Belov:** Resources. **F. Bisconti:** Validation. **C. Blaksley:** Validation. **S. Blin:** Validation, Resources. **F. Capel:** Validation, Resources. **M. Casolino:** Validation, Supervision, Project administration, Investigation, Funding acquisition. **I. Churilo:** Funding acquisition. **A.G. Coretti:** Validation. **M. Crisconio:** Funding acquisition. **C. De La Taille:** Resources. **T. Ebisuzaki:** Resources, Project administration, Funding acquisition. **F. Fenu:** Validation, Software, Resources, Investigation. **M.A. Franceschi:** Resources. **C. Fuglesang:** Validation. **S. Gallian:** Supervision, Resources, Methodology. **D. Gardiol:** Resources. **A. Golzio:** Writing – original draft, Validation, Supervision, Software, Resources. **P. Gorodetzky:** Project administration. **F. Kajino:** Validation. **H. Kasuga:** Resources. **P. Klimov:** Validation, Resources, Project administration, Investigation, Funding acquisition. **V. Kungel:** Resources, Methodology, Investigation. **V. Kuznetsov:** Funding acquisition. **M. Manfrin:** Data curation. **L. Marcelli:** Validation, Resources, Investigation, Data curation. **W. Marszał:** Resources. **G. Mascetti:** Funding acquisition. **M. Mignone:** Resources, Data curation. **H. Miyamoto:** Validation, Software, Methodology, Investigation, Formal analysis, Data curation, Conceptualization. **A. Murashov:** Resources. **T. Napolitano:** Resources. **H. Ohmori:** Resources. **A. Olinto:** Funding acquisition. **P. Picozza:** Project administration, Funding acquisition. **L.W. Piotrowski:** Validation, Software, Resources, Data curation. **Z. Plebaniak:** Writing – original draft, Visualization, Validation, Supervision, Software, Resources, Investigation, Data curation, Conceptualization. **G. Prévôt:** Resources, Investigation, Funding acquisition. **E. Reali:** Resources, Conceptualization. **F. Reynaud:** Investigation. **M. Ricci:** Validation, Supervision, Resources, Project administration, Investigation, Funding acquisition. **G. Romoli:** Resources, Investigation. **S. Sharakin:** Resources, Data curation. **K. Shinozaki:** Software, Conceptualization. **J.**

Szabelski: Validation, Resources. **Y. Takizawa:** Validation, Resources, Data curation. **V. Vagelli:** Validation, Funding acquisition. **G. Valentini:** Resources, Funding acquisition. **M. Vrabel:** Visualization, Validation, Software, Resources, Investigation, Data curation. **L. Wiencke:** Resources, Investigation, Funding acquisition, Conceptualization. **M. Zotov:** Validation.

Declaration of competing interest

The authors declare that they have no known competing financial interests or personal relationships that could have appeared to influence the work reported in this paper.

Acknowledgments

This work was supported by the Italian Space Agency (ASI) through the agreement between ASI and University of Roma Tor Vergata n. 2020-26-HH.0, by the French space agency CNES, and by the National Science Centre in Poland grants 2017/27/B/ST9/2162 and 2020/37/B/ST9/01821. This research has been supported by Russian State Space Corporation Roscosmos. The article has been prepared based on research materials collected in the space experiment "UV atmosphere". We thank the Altea-Lidal collaboration for providing the orbital data of the ISS. The authors also thank the PRISMA project, the Italian Network for Systematic surveillance of Meteors and Atmosphere, for providing the data collected during the observation night. PRISMA is a collaboration initiated and coordinated by the Italian National Institute for Astrophysics (INAF) that counts members among research institutes, associations, and schools. The complete list of PRISMA members is available at http://www.prisma.inaf.it. Finally, the authors thank the Mini-EUSO team and the JEM-EUSO members.

Appendix A. Flat fielding procedure

In this appendix, we recall the Mini-EUSO flat fielding procedure, using the quantities defined in this paper. The plots shown are produced using the data of the orbit of the first flasher observation, on May 4th 2021 (Session 40).

A.1. Flat field

A complete description of the flat field algorithm is already reported in [19], here the basic aspects will be summarized, with a particular focus on the parametrization of the flat field values.

Fig. A.27 shows an example of Mini-EUSO data before and after the flat field procedure. The frame was taken when Mini-EUSO was observing the ocean off the coast of Africa, therefore the background is quite uniform apart from the presence of a few cloud structures. From the top panel it is possible to appreciate the large variability in the pixels' photon counts (and therefore in their efficiency η_i). The bottom panel instead shows the same frame after flat fielding, where the PDM output is much more uniform, and fainter details, like the presence of cloud patches, are visible. This demonstrates the accuracy of the flat fielding procedure in compensating for the different pixel efficiencies.

The flat field values for each pixel are obtained under the assumption that, although all pixels do not observe the same light intensity at any given time (because of the spatial variability of the ground emissivity over the instrument's FoV), the minimum background light that they observe over a complete orbit is essentially the same (which may typically correspond to ocean, desert or forest areas). Under this assumption, the ratios of the photon counts corresponding to this minimum counting rate, $N_i^{\min}$, provide an indirect measurement of the relative efficiency ratios of the different pixels. Fig. A.28 shows the histogram of the photon counts of two neighboring pixels, which observe almost the same environment throughout an orbit. To avoid low statistics measurement fluctuations, it proves appropriate to choose

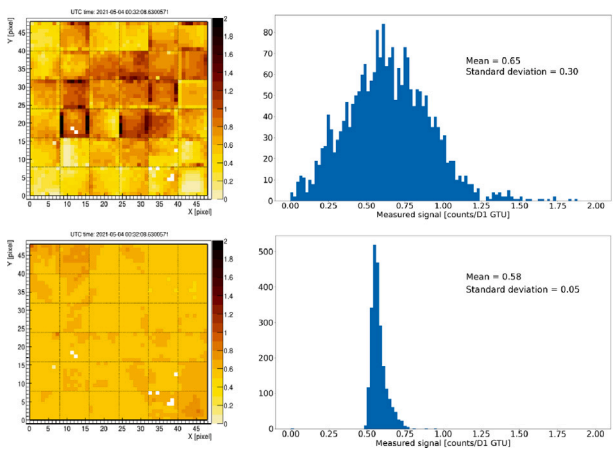

Fig. A.27. Top Left: Data taken off the coast of Africa, 850 km south of Cape Verde (Lat: 7.126, Lon: −23.334). The different photon counts in each pixel are mainly due to the different efficiencies of the pixels. **Top Right:** histogram of the photon counts registered in the 2304 pixels. **Bottom Left:** the same data shown above, after the flat fielding procedure. Details like the slightly more bright patches produced by the clouds, are visible. **Bottom Right:** histogram of the flat-fielded data. Also in this case the spread is significantly reduced. The right tail is due to the presence of clouds.

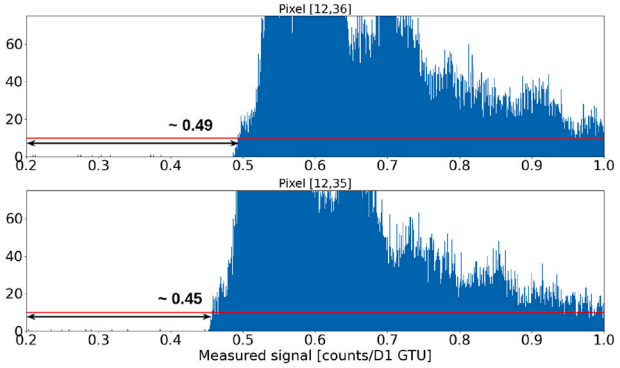

Fig. A.28. Histogram of the photon counts registered by two neighboring pixels. Being one above the other, they observe almost the same environment. Nevertheless, pixel [12,36] (top panel) presents higher photon counts than the other. The lowest background value (red horizontal line) is $N^{\min}_{[12,36]} \simeq 0.49$ counts/GTU for pixel [12,36] while it has a higher value of $N^{\min}_{[12,35]} \simeq 0.45$ counts/GTU for pixel [12,35]. The two different responses are normalized to unity by dividing the photon counts of each pixel in each GTU by these factors.

as the reference minimum photon counts not the very lowest photon counts recorded by a given pixel, but the photon counts recorded a given (small) number of times during the orbit. In practice, we use the minimum photon counts appearing at least ten times in the histogram, as shown by the horizontal red lines in Fig. A.28. The corresponding photon counts, highlighted by the black arrows, are then used to represent $N_i^{\min}$. The different values are thus assumed to directly reflect the different efficiencies of the pixels. For each pixel, a rescaling factor is then derived to compensate for the different efficiencies, defined as

$$\mathrm{FF}_i = \frac{N_i^{\min}}{\langle N_k^{\min} \rangle_{k \in \mathrm{RPs}}}, \tag{A.1}$$

where the average in the denominator is taken over a subset of pixels, referred to as the Representative Pixels (RPs), which are identified as the most stable pixels from one orbit to another, in the sense that their relative minimum photon counts $N_k^{\min}/N_l^{\min}$ are essentially the same, whatever the orbit, for any two pixels, k and l among them. In other words, although their actual minimum photon counts vary from one orbit to another (mostly due to different levels of moon light

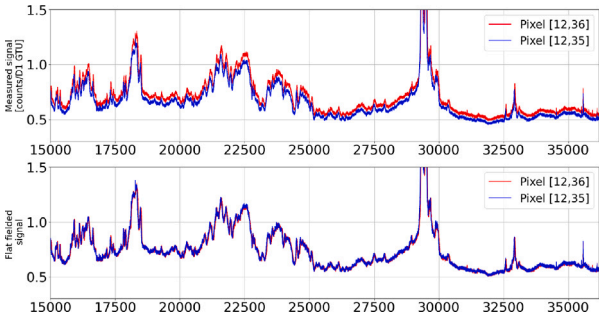

Fig. A.29. Lightcurve of the two neighboring pixels considered in Fig. A.28 as a function of time. **Top panel:** uncorrected signal data; **Bottom panel:** flat-fielded data.

reflection), they vary together, mostly proportionally to one another. The application of this rescaling factor is shown in the bottom panels of Fig. A.27 (for a single GTU) and Fig. A.29 (for the lightcurves of two neighboring pixels).

The measured minimum photon counts of a given pixel, $N_i^{\min}$, does not only depend on its efficiency and on the emissivity of the region it is observing, but also on geometrical parameters and the transmittance of the atmosphere, as summarized by Eq. (14). Based on that, the minimum background level observed by pixel i can be expressed as:

$$N_i^{\min} = \left(\mathcal{E}_0\, \Delta t_{\rm GTU}\, \Omega_i\, T_i^{(\rm atm)}\, S_i\, T_i^{(\rm optics)}\, \xi_i\right)_{\min} \tag{A.2}$$

or, using the parametrization for

$$T_i^{(\rm optics)}\, \xi_i = \eta_i, \qquad \text{(Eq. (18))},$$

$$\Omega_i = \frac{S_{\rm window} \cos^3 \Theta_i}{H_{\rm ISS}^2}, \qquad \text{(Eq. (4))},$$

$$T_i^{(\rm atm)} = T_{0^\circ}^{(\rm atm)}\; L_i^{(\rm atm)}, \qquad \text{(Eq. (33))},$$

we can rewrite it in the alternative form:

$$N_i^{\min} = \left(\frac{\mathcal{E}_0\; T_{0^\circ}^{(\rm atm)}}{H_{\rm ISS}^2}\right)_{\min} \times \Delta t_{\rm GTU}\; S_{\rm window} \times S_i\; L_i^{(\rm atm)}\; \cos^3\theta_i\; \eta_i. \tag{A.3}$$

The first term of the equation is made of time-dependent factors, the second term of constant factors, and the third part of pixel-dependent factors.[3] In other words, the evolution of the first term describes how the light collected by a single pixel changes in time (namely, the lightcurve), while the third term describes the differences among the pixels (namely, the variability shown in the top panel of Fig. A.27).

Under the aforementioned assumption that the minimum background light that each pixel observes over a complete orbit, expressed by the first term of Eq. (A.3), is essentially the same, the denominator of Eq. (A.1), $\langle N_k^{\min}\rangle_{k\in \rm RPs}$, can be expressed by the same formulation of Eq. (A.3) only by changing the third term with an average over the representative pixels

$$\langle S_k\; L_k^{(\rm atm)}\; \cos^3\theta_k\; \eta_k\rangle_{k\in \rm RPs}$$

With that result, we can rewrite Eq. (A.1) as a simple ratio:

$$\mathrm{FF}_i = \frac{S_i\; L_i^{(\rm atm)}\; \cos^3\theta_i\; \eta_i}{\langle S_k\; L_k^{(\rm atm)}\; \cos^3\theta_k\; \eta_k\rangle_{k\in RPs}} \tag{A.4}$$

This formulation explicitly shows that the flat field makes the output of all the pixels uniform, compensating not only for the differences in the pixels' efficiency but also for the parameters depending on the viewing angle θ

[3] Strictly speaking, the factors S_i, $L_i^{(\rm atm)}$ and θ_i depend on the ISS attitude angles that can slowly change with time. This effect is however negligible with respect to the time variation of the first term of the equation.

A.1.1. Applying the flat field to diffuse light sources

Eq. (14) gives, under reasonable assumptions, the photon counts obtained by pixel i in case of uniform and diffuse background. The same equation can describe the photon counts by any diffuse light source simply by changing the factor $\mathcal{E}_0$ with a general $\mathcal{E}(\theta, \phi, \vec{r}, t, \ldots)$, provided that the emission is constant over an area significantly larger than the footprint of one or few pixels. In this case, the flat fielded counts $N_i^{\rm FF}$ obtained by dividing by Eq. (A.4) can be expressed as

$$N_i^{\rm FF} = \frac{N_i}{\mathrm{FF}_i} = \frac{\mathcal{E}(\theta, \phi, \vec{r}, t, \ldots)\; T_{0^\circ}^{(\rm atm)}}{H_{\rm ISS}^2} \times \Delta t_{\rm GTU}\; S_{\rm window} \times \langle S_l\; L_l^{(\rm atm)}\; \cos^3\theta_l\; \eta_l\rangle_{l\in RPs} \tag{A.5}$$

Note that the final results no longer depend on i. In this case, applying the flat field means using for all the pixels the value of the quantities in Eq. (A.4), averaged over the representative pixels. The result should be the same for all the pixels observing the same diffuse source.

Appendix B. Weather conditions during Sant'Antimo Abbey field measurements

During MiniEUSO session 71 (30th October 2022) the ISS crossed the night sky over Italy between 3:42 and 3:45 CEST and the flasher was positioned at Sant'Antimo Abbey in Tuscany. During that night the sky condition forecast by the automatic procedure that uses the Global Forecasting System data (NCEP) is depicted in Fig. B.30, where the times are expressed in UTC. Fig. B.30 depicts the total cloud cover in 30 min of trajectory, the light blue over central Italy shows the absence of clouds on the entire atmospheric column. As long as this represents a forecast, very useful to plan the field measurements, we inspected also the geostationary satellite image (Fig. B.31) that shows the absence of clouds and fog over Central and Southern Italy when the ISS flight over (see Fig. 13).

Appendix C. Weather conditions in the area according to the measurement of PRISMA cameras

To further confirm the weather conditions of the sky during the night of the Sant'Antimo Abbey field measurements, we used the all-sky measurements of the PRISMA fireball network. Such measurements are also able to provide an estimation of the atmospheric extinction coefficient (which is related to the transmittance $T_{0^\circ}^{(\rm atm)}$ along the zenith direction, see Section 10.1) but in a wavelength range different to the one of Mini-EUSO.

PRISMA[4] is an experiment devoted to the detection of bright meteors (*i.e.* fireballs or bolides) over the Italian territory [17,18] and it is a partner of the FRIPON[5] international collaboration [32]. The main scientific objectives of PRISMA are the study of the source regions of meteoroids impacting the Earth's atmosphere and the determination of the area of fall (*i.e.* strewn-field) of meteorite specimens if a significant fraction of the pre-atmospheric mass of the meteoroid survives the atmospheric transit. In order to pursue such objectives, PRISMA implemented about 70 fireball-monitoring stations in Italy. Each station mainly consists of an all-sky camera, able to image the whole visible hemisphere in one frame thanks to a fish-eye objective, that is operated by mini-PC at a frequency of 30 Hz in order to trigger

[4] PRISMA is an acronym that, in Italian, stands for "Prima Rete Italiana per la Sorveglianza sistematica di Meteore ed Atmosfera" and that can be translated in English as "First Italian Network for the systematic Surveillance of Meteors and the Atmosphere".

[5] FRIPON is an acronym that stands for Fireball Recovery and InterPlanetary Observation Network

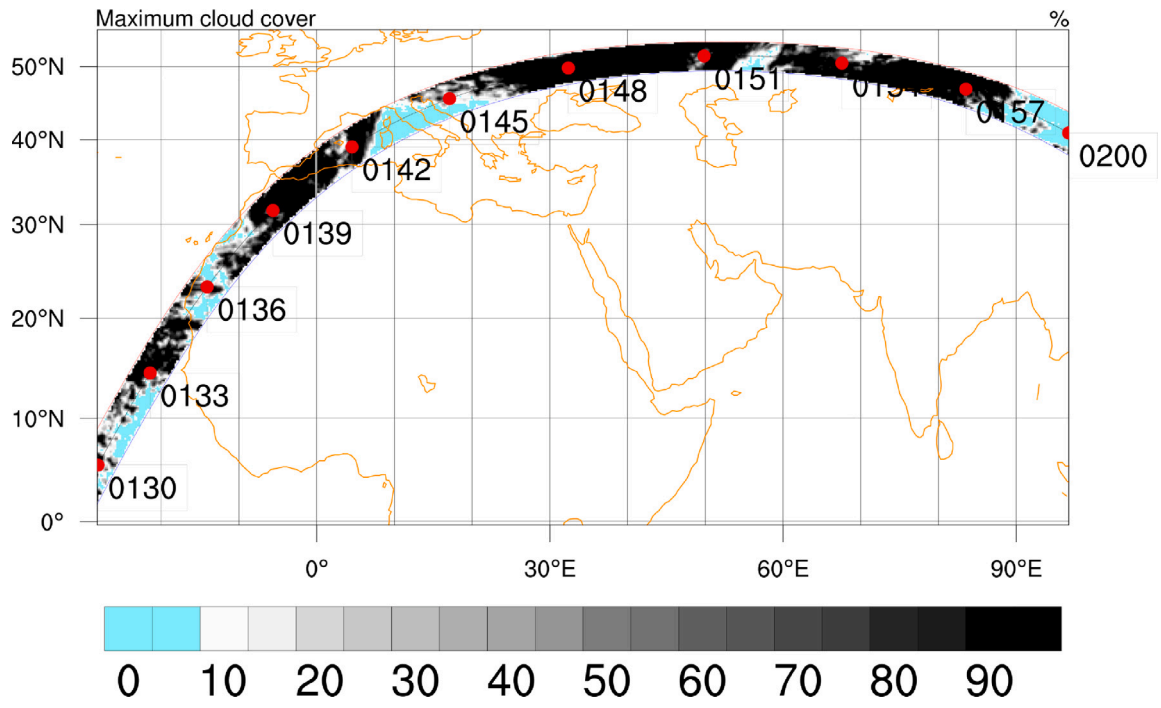

Fig. B.30. The weather forecast from GFS along the predicted trajectory of ISS. The forecast is 30 min long, the central part, around 1:45 UTC, crossed central Italy, and the total cloud cover was below 10%, indicating clear-sky conditions.

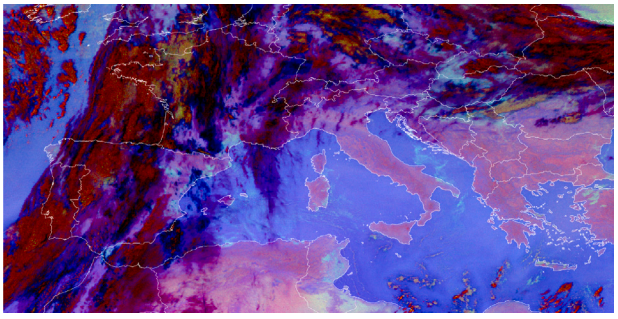

Fig. B.31. Geostationary meteorological satellite Meteosat positioned at 0° E over the equator at 36 000 km from Earth's surface (30 October 2022 at 1:45 UTC). The image is an RGB product composed of data from a combination of the SEVIRI IR3.9, IR10.8 and IR12.0 channels, and it is useful during the night to detect possible low-level clouds or fog, however also all the other cloud layers are visible (e.g. on Western France). Light purple over central Italy indicates the clear-sky condition.

for the transit of meteor events in the FoV of the camera, sampling their visible trajectory at a suitable rate. Since the start of the project, the observations of PRISMA enabled the recovery of two freshly-fallen meteorites, namely Cavezzo[6] in January 2020 and Matera[7] in February 2023.

For calibration purposes, each PRISMA station continuously acquires a set of long-exposure (5 s) images every 10 min. On these images acquired during night-time, stars are visible up to +4.5 magnitude in the V wavelength bandpass if weather conditions and cloud coverage are favorable. The analysis of this dataset, for each station and for each night of observation, is then used to derive the astrometric and photometric calibration of the CCD sensor and the optical system, by comparing the measured position and intensity of each star with its catalogue values [33]. In particular, the photometric calibration processing [34] evaluates the residuals between experimental (m_s) and catalogue (m) magnitude values for each identified star as:

$$\Delta m = m - m_s = C - kX \ , \tag{C.1}$$

where C is the photometric zero-point magnitude that encloses the term of the sensor efficiency, k is the atmospheric extinction coefficient (given in magnitude per airmass units) and X is the airmass, *i.e.* the amount of air along the line of sight relative to the one along the zenith direction (parametrized through the formulation of [35]). To solve Eq. (C.1) against PRISMA measure of stars brightness, we refer to the Hipparcos catalogue [36] and, in particular, to its H_p broadband magnitude that provides the closest match with the bandpass of the PRISMA sensors. Therefore, the transmittance $T^{(\mathrm{atm})}_{0°}$ in the zenith direction defined in Section 10.1 can be expressed as a function of k as:

$$T^{(\mathrm{atm})}_{0°} = 10^{-0.4k} \ . \tag{C.2}$$

Given that k is estimated through the analysis of Eq. (C.1) with stars up to $X \simeq 4.5$, *i.e.* down to ∼13° above the horizon, $T^{(\mathrm{atm})}_{0°}$ estimated through Eq. (C.2) represents an average value of the transmittance in an atmospheric cone with an aperture of 154° and its vertex positioned on the geographic location of the station.

Considering the night of the Mini-EUSO session 71 (29th–30th October 2022), for which the flasher was positioned at the Sant'Antimo Abbey in Tuscany, the closest active stations of the PRISMA network were ITTO05 - Chianti (43.52374°N, 11.24574°E) and ITUM02 - Amelia (42.53230°N, 12.38647°E), at a distance from the flasher position of 63 km and 87 km, respectively. Two other PRISMA stations (ITTO06 - Piombino and ITUM01 - Perugia) were active that night. Still, the plastic dome protecting the sensor of both these cameras presented a layer of dust and water droplets from precipitation the days before and, as a consequence, photometric measurements were not possible. Fig. C.32 shows the results of the fit of Eq. (C.1) against the data of ITTO05 and ITUM02, which encompasses $\sim 10^4$ and 1.2×10^4 measurements of stars during that night, respectively. The derived values of the atmospheric extinction coefficient are $k_1 = 0.167 \pm 0.010$ ($T^{(\mathrm{atm})}_{0°,1} = 85.7 \pm 0.8\%$) for ITTO05 and $k_2 = 0.175 \pm 0.007$ ($T^{(\mathrm{atm})}_{0°,2} = 85.1 \pm 0.5\%$) for ITUM02.

[6] https://www.lpi.usra.edu/meteor/metbull.php?code=72534.
[7] https://www.lpi.usra.edu/meteor/metbull.php?code=81326.

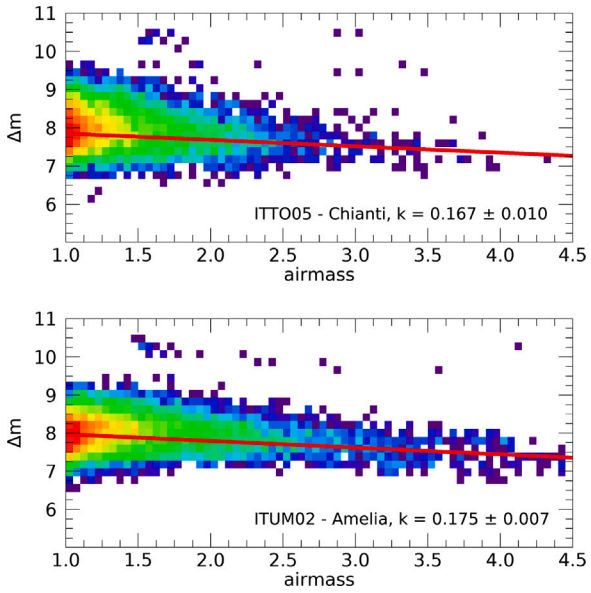

Fig. C.32. Results of the photometric calibration of the ITTO05 - Chianti (top panel) and ITUM02 - Amelia (bottom panel) cameras of the PRISMA network for the night of the Mini-EUSO session 71 (29th–30th October 2022) for $\sim 10^4$ and 1.2×10^4 identified stars, respectively. Both panels report the density plot of magnitude residuals $\Delta m = m - m_s$, in logarithmic color scale, as a function of the airmass of observed stars in the FoV. The red line plots the fit of Eq. (C.1) for the determination of the photometric zero-point magnitude (C) and the atmospheric extinction coefficient (k).

All stars that are detected by each camera (*i.e.*, for visual magnitudes $V \lesssim +4.5$) in its field of view are considered altogether for this analysis. In such a case, Eq. (C.1) should include color terms that account for the differential extinction for stars with different spectral types. Nevertheless, PRISMA can measure stellar magnitudes with 0.2 mag of precision only, and this is not enough to perform such more precise calibration (which is usually on this order of magnitude, or less). That being said, since no selection criteria are applied, such analysis encompasses stars with all spectral types. Therefore, the value of the atmospheric extinction coefficient k (and $T_{0°}^{(\mathrm{atm})}$) resulting from this analysis is to be considered averaged for all the stars (and all the spectral types) observed during that night by each camera.

The same processing was repeated for the calibration data acquired by the two considered PRISMA stations during a time interval of one month before and after the date of the flashed campaign at the Sant'Antimo Abbey in Tuscany, from September to November 2022. This further analysis highlighted that, in this region of Italy, the atmospheric conditions during the night of the Mini-EUSO session 71 were exceptionally good. In particular, the value of the atmospheric extinction coefficient determined for that night of $k \simeq 0.17$ is at the lower end of the distribution of k on the considered period, which ranges from 0.15 to 0.4 and corresponds to a variability of the atmospheric transmittance from 70% to 87%. Moreover, the median value of the sky magnitude at the zenith direction of ~19.5 mag/arcsec^2 is particularly high, indicating a cloud-free night when compared to its overall variability from 16 to 19.5 mag/arcsec^2; however, this variability also depends on the Moon phase and the local conditions of light pollution at the observation site. These conclusions are in agreement with the results of the GFS forecast and satellite observations presented in Appendix B, highlighting the absence of clouds and fog over Central and Southern Italy.

Taking a step further, one may attempt to compare the experimental results of the atmospheric transmittance measured by PRISMA cameras against the output of the libRadtran package, assuming the AOD data by the MODIS satellite spectrometer, that was used to estimate the atmospheric transmittance for the Mini-EUSO measurements of the LED flasher (see Section 10.1). However, the results of PRISMA refer to the wide bandpass of the PRISMA camera that covers wavelengths from 250 nm to 1100 nm (with a maximum at ~500 nm, see Fig. 3 of [34]) and, therefore, they are not directly applicable to the experimental case of Mini-EUSO that observes the LED flasher signal peaked at 400 nm (Section 10.1). To compare these results to the output of libRadTran, we considered an average of the transmittance as a function of wavelength for nadir observations (Fig. 21, top panel, but computed for the coordinates of ITTO05 and ITUM02) weighted by the efficiency curve of PRISMA cameras. The results of the average transmittance according to this computation are $81.5^{+2.9}_{-4.5}$% for ITTO05 and $81.0^{+3.2}_{-4.5}$% for ITUM02. The corresponding 95% confidence intervals of these simulated values overlap with the results of PRISMA measurements mentioned above. Such evidence confirms that the estimation of the atmospheric transmittance obtained through libRadtran and assuming the AOD estimations can be considered reliable and, for our case, they are validated against experimental results of PRISMA.

Data availability

Data will be made available on request.

References

[1] K. Kotera, A. Olinto, The astrophysics of ultrahigh energy cosmic rays, Ann. Rev. Astron. Astrophys. 49 (2011) 119–153.

[2] A. Aab, P. Abreu, M. Aglietta, et al., Measurement of the cosmic-ray energy spectrum above 2.5×10^{18} eV using the Pierre Auger Observatory, Phys. Rev. D 102 (2020) 062005.

[3] A. Coleman, et al., Ultra high energy cosmic rays the intersection of the cosmic and energy frontiers, Astropart. Phys. 149 (2023) 102819, http://dx.doi.org/10.1016/j.astropartphys.2022.102794, arXiv:2205.05845.

[4] E. Parizot, et al., The JEM-EUSO program for UHECR studies from space, EPJ Web Conf. 283 (2023) 06007, http://dx.doi.org/10.1051/epjconf/202328306007.

[5] G. Abdellaoui, S. Abe, J. Adams Jr., et al., EUSO-TA – first results from a ground-based EUSO telescope, Astropart. Phys. 102 (2018) 98–111.

[6] J. Adams Jr., S. Ahmad, J.-N. Albert, et al., The EUSO-balloon pathfinder, Exp. Astron. 40 (2015) 281–299.

[7] G. Abdellaoui, et al., JEM-EUSO, EUSo-SPB1 mission and science, Astropart. Phys. 154 (2024) 102891, http://dx.doi.org/10.1016/j.astropartphys.2023.102891.

[8] J. Adams Jr., L. Anchordoqui, J. Apple, et al., White paper on EUSO-SPB2, 2017, arXiv:1703.04513.

[9] P.A. Klimov, et al., The TUS detector of extreme energy cosmic rays on board the lomonosov satellite, Space Sci. Rev. 212 (3) (2017) 1687–1703, http://dx.doi.org/10.1007/s11214-017-0403-3, arXiv:1706.04976.

[10] S. Bacholle, P. Barrillon, M. Battisti, et al., Mini-EUSO mission to study earth UV emissions on board the ISS, Astrophys. J. Suppl. Ser. 253 (2) (2021) http://dx.doi.org/10.3847/1538-4365/abd93d.

[11] M. Battisti, J. Eser, A. Olinto, G. Osteria, POEMMA-balloon with radio: A balloon-born multi-messenger multi-detector observatory, Nucl. Instrum. Methods Phys. Res. A 1069 (2024) 169819, http://dx.doi.org/10.1016/j.nima.2024.169819.

[12] M. Battisti, J. Eser, G. Filippatos, A. Olinto, G. Osteria, E. Parizot, The fluorescence camera of the POEMMA-balloon with radio (PBR): Design and scientific goals, Nucl. Instrum. Methods Phys. Res. A 1068 (2024) 169727, http://dx.doi.org/10.1016/j.nima.2024.169727.

[13] P.A. Klimov, et al., Status of the K-EUSO orbital detector of ultra-high energy cosmic rays, Universe 8 (2) (2022) 88, http://dx.doi.org/10.3390/universe8020088, arXiv:2201.12766.

[14] A. Olinto, J. Krizmanic, J. Adams Jr., et al., The POEMMA (probe of extreme multi-messenger astrophysics) observatory, J. Cosmol. Astrop. Phys. 6 (2021) 007.

[15] J. Adams Jr., S. Ahmad, J.-N. Albert, et al., The JEM-EUSO mission: An introduction, Exp. Astron 40 (2015) 3–17.

[16] L. Wiencke, et al., The JEM-EUSO global light system, in: Proc. 33rd Int. Cosmic Ray Conf., Vol. 0818, 2013, arXiv:1307.7071.

[17] D. Gardiol, et al., News from the Italian PRISMA fireball network, in: R. Rudawska, J. Rendtel, C. Powell, R. Lunsford, C. Verbeeck, A. Knöfel (Eds.), Proceedings of the 37th International Meteor Conference Pezinok-Modra, Slovakia, 30 August - 2 September 2018, 2019, pp. 81–86.

[18] D. Gardiol, D. Barghini, et al., Cavezzo, the first Italian meteorite recovered by the PRISMA fireball network. Orbit, trajectory, and strewn-field, Mon. Not. R. Astron. Soc. 501 (1) (2021) 1215–1227, http://dx.doi.org/10.1093/mnras/staa3646.

[19] M. Casolino, et al., Observation of night-time emissions of the earth in the near UV range from the international space station with the mini-EUSO detector, Remote Sens. Environ. 284 (2023) 113336, http://dx.doi.org/10.1016/j.rse.2022.113336, arXiv:2212.02353.

[20] M. Battisti, et al., Analysis of EAS-like events detected by the mini-EUSO telescope, PoS ICRC2023 (2023) 353, http://dx.doi.org/10.22323/1.444.0353.

[21] L. Marcelli, et al., Observation of ELVES with mini-EUSO telescope on board the international space station, PoS ICRC2021 (2021) 367, http://dx.doi.org/10.22323/1.395.0367.

[22] A. Belov, et al., The integration and testing of the mini-EUSO multi-level trigger system, Adv. Space Res. 62 (10) (2018) 2966–2976, http://dx.doi.org/10.1016/j.asr.2017.10.044, arXiv:1711.02376.

[23] M. Battisti, et al., Onboard performance of the level 1 trigger of the mini-EUSo telescope, Adv. Space Res. 70 (9) (2022) 2750–2766, http://dx.doi.org/10.1016/j.asr.2022.07.077.

[24] D. Barghini, et al., Observation of meteors from space with the mini-EUSO detector on board the international space station, Astron. Astrophys. (2024) http://dx.doi.org/10.1051/0004-6361/202449236.

[25] V. Kungel, et al., UV laser system test of mini-EUSO, in: In Proc. 36rd Int. Cosmic Ray Conf., Vol. 358, 2019, http://dx.doi.org/10.22323/1.358.0325, arXiv:1909.04279.

[26] H. Miyamoto, et al., An end-to-end in-flight calibration of mini-EUSO detector, EPJ Web Conf. 283 (2023) 06017, http://dx.doi.org/10.1051/epjconf/202328306017.

[27] Ophir Optronics, 300 mW UV-Silicon Photodiode Sensor with 10x10 mm Aperture. https://www.ophiropt.com/en/f/pd300-uv-photodiode-sensor.

[28] P. Barrillon, et al., The EUSo@TurLab project in the framework of the JEM-EUSO program, Exp. Astron. 55 (2) (2023) 569–602, http://dx.doi.org/10.1007/s10686-022-09871-8.

[29] C. Emde, R. Buras-Schnell, A. Kylling, B. Mayer, J. Gasteiger, U. Hamann, J. Kylling, B. Richter, C. Pause, T. Dowling, L. Bugliaro, The libradtran software package for radiative transfer calculations (version 2.0.1), Geosci. Model Dev. 9 (5) (2016) 1647–1672, http://dx.doi.org/10.5194/gmd-9-1647-2016, URL: https://gmd.copernicus.org/articles/9/1647/2016/.

[30] B. Mayer, A. Kylling, Technical note: The libradtran software package for radiative transfer calculations - description and examples of use, Atmos. Chem. Phys. 5 (7) (2005) 1855–1877, http://dx.doi.org/10.5194/acp-5-1855-2005, URL: https://acp.copernicus.org/articles/5/1855/2005/.

[31] R.C. Levy, S. Mattoo, L.A. Munchak, L.A. Remer, A.M. Sayer, F. Patadia, N.C. Hsu, The collection 6 MODIS aerosol products over land and ocean, Atmos. Meas. Tech. 6 (11) (2013) 2989–3034, http://dx.doi.org/10.5194/amt-6-2989-2013, URL: https://amt.copernicus.org/articles/6/2989/2013/.

[32] F. Colas, et al., FRIPON: a worldwide network to track incoming meteoroids, Astron. Astrophys. 644 (2020) A53, http://dx.doi.org/10.1051/0004-6361/202038649, arXiv:2012.00616.

[33] D. Barghini, D. Gardiol, A. Carbognani, S. Mancuso, Astrometric calibration for all-sky cameras revisited, Astron. Astrophys. 626 (2019) A105, http://dx.doi.org/10.1051/0004-6361/201935580.

[34] D. Barghini, D. Gardiol, A. Carbognani, Improving astrometry and photometry reduction for PRISMA all-sky cameras, in: R. Rudawska, J. Rendtel, C. Powell, R. Lunsford, C. Verbeeck, A. Knofel (Eds.), International Meteor Conference, Pezinok-Modra, Slovakia, 2019, pp. 41–45.

[35] G.V. Rozenberg, Reviews of topical problems: Twilight phenomena, their nature, and use for atmospheric research, Sov. Phys. Usp. 6 (2) (1963) 198–249, http://dx.doi.org/10.1070/PU1963v006n02ABEH003505.

[36] M.A.C. Perryman, et al., The HIPPARCOS catalogue, Astron. Astrophys. 323 (1997) L49–L52.